The Astrophysical Journal, 833:201 (29pp), 2016 December 20 doi:10.3847/1538-4357/833/2/201

RADIATIVE TRANSFER MODEL OF DUST ATTENUATION CURVES IN CLUMPY, GALACTIC ENVIRONMENTS

Kwang-Il Seon[1,2,3] and Bruce T. Draine[2]
[1] Korea Astronomy and Space Science Institute, Daejeon, 305-348, Korea; kiseon@kasi.re.kr
[2] Department of Astrophysical Sciences, Princeton University, Princeton, NJ, 08544, USA
[3] Astronomy and Space Science Major, Korea University of Science and Technology, Daejeon, 305-350, Korea
Received 2016 June 6; revised 2016 October 6; accepted 2016 October 28; published 2016 December 19

ABSTRACT

The attenuation of starlight by dust in galactic environments is investigated through models of radiative transfer in a spherical, clumpy interstellar medium (ISM). We show that the attenuation curves are primarily determined by the wavelength dependence of absorption rather than by the underlying extinction (absorption+scattering) curve; the observationally derived attenuation curves cannot constrain a unique extinction curve unless the absorption or scattering efficiency is specified. Attenuation curves consistent with the "Calzetti curve" are found by assuming the silicate-carbonaceous dust model for the Milky Way (MW), but with the 2175 Å bump suppressed or absent. The discrepancy between our results and previous work that claimed the Small Magellanic Cloud dust to be the origin of the Calzetti curve is ascribed to the difference in adopted albedos; we use the theoretically calculated albedos, whereas the previous works adopted albedos derived empirically from observations of reflection nebulae. It is found that the attenuation curves calculated with the MW dust model are well represented by a modified Calzetti curve with a varying slope and UV bump strength. The strong correlation between the slope and UV bump strength, as found in star-forming galaxies at $0.5 < z < 2.0$, is well reproduced when the abundance of the UV bump carriers is assumed to be 30%–40% of that of the MW dust; radiative transfer effects lead to shallower attenuation curves with weaker UV bumps as the ISM is more clumpy and dustier. We also argue that some local starburst galaxies have a UV bump in their attenuation curves, albeit very weak.

Key words: dust, extinction – methods: numerical – radiative transfer – scattering

1. INTRODUCTION

Spectral energy distributions (SEDs) of galaxies provide crucial information on stellar populations, metal content, and star formation history (e.g., Kennicutt 1998; Conroy 2013). However, internal dust absorbs and scatters starlight, thereby hampering our ability to directly measure the intrinsic SEDs of galaxies, especially at ultraviolet (UV) wavelengths. Quantifying the dust attenuation effect is, therefore, essential in deriving the intrinsic properties of galaxies from the observed SEDs. It also helps us understand the nature of dust grains and the star/dust geometry.

The dust attenuation for extended objects, such as external galaxies, should be distinguished from the extinction for individual point sources. The extinction represents the loss of starlight out of the observer's line of sight as a result of both absorption and scattering. Extinction curves as a function of wavelength have been measured only for the Milky Way (MW; Fitzpatrick 1999), the Large Magellanic Cloud (LMC; Misselt et al. 1999), the Small Magellanic Cloud (SMC; Gordon & Clayton 1998), and M31 (Bianchi et al. 1996; Clayton et al. 2015), where individual stars are resolved, and for galaxies in front of quasi-stellar objects (QSOs) and gamma-ray bursts (GRBs) (Elíasdóttir et al. 2006, 2009). The attenuation, in contrast, is defined as net loss of starlight that is due to complex radiative transfer effects of the underlying dust extinction properties and spatial distributions of dust and stars. The attenuation is sometimes referred to as the effective extinction.

To quantify the attenuation effect, Kinney et al. (1994) estimated a dust attenuation curve from the UV to the near-infrared (NIR) for two local starburst galaxies, which were assumed to share the same stellar populations, by dividing the spectrum of the more reddened galaxy with that of the less reddened galaxy. By applying a similar method to a sample of 39 local starburst and blue compact galaxies, Calzetti et al. (1994, 2000) derived a mean attenuation curve, which is now referred to as the Calzetti attenuation curve or the Calzetti law. More recently, Battisti et al. (2016) applied the method of Calzetti et al. (1994, 2000) to a sample of ∼10,000 local ($z \lesssim 0.1$) star-forming galaxies obtained from *GALEX* and *SDSS* and found that an attenuation curve derived from the sample is consistent with the Calzetti curve for local starburst galaxies. Attenuation curves covering the far-UV wavelength shortward of 0.12 μm were also derived for local starburst galaxies (Leitherer et al. 2002) and for galaxies at $z \sim 3$ (Reddy et al. 2016); the far-UV attenuation curves are similar to the Calzetti curve at $\lambda \gtrsim 0.12$ μm, but shallower than the extrapolation of the Calzetti curve at $\lambda \lesssim 0.12$ μm. Charlot & Fall (2000) found that an attenuation curve proportional to $\lambda^{-0.7}$ reproduces the relation between the ratio of far-infrared (FIR) to UV luminosities and the UV spectral slope observed in local starburst galaxies. The Calzetti curve somewhat resembles a power law $\lambda^{-0.7}$ (e.g., Kauffmann et al. 2003). These attenuation curves have been the most commonly adopted for modeling the stellar populations of high-redshift galaxies. The most prominent characteristics of both attenuation curves are the absence of the UV absorption bump at 2175 Å, which is commonly visible in the MW and LMC, and a grayer (shallower) slope than the average MW extinction curve.

The absence of a UV absorption bump in the Calzetti attenuation curve motivated the radiative transfer studies of Gordon et al. (1997) and Witt & Gordon (2000) to investigate the nature of dust grains in local starburst galaxies. By varying the underlying extinction curve and star/dust geometries, they

concluded that the dust in local starburst galaxies has an SMC-like extinction curve lacking a 2175 Å bump. Using the same model, Gordon et al. (1999b) also showed that color–color plots, suitable to probe the presence ot lack of the 2175 Å bump, of starburst galaxies at $z = 1$–3 in the Hubble Deep Fields (HDFs) are consistent with SMC-like dust. The far-UV (FUV) slope (observed $G - \mathcal{R}$ color) of a large sample of Lyman-break galaxies (LBGs) at $z \sim 3$ was also found to be consistent with an SMC-like extinction curve (Vijh et al. 2003). For a sample of ∼1000 galaxies with UV-to-IR photometry and optical spectroscopy, Johnson et al. (2007) derived mean low-resolution attenuation curves that are consistent with both a $\lambda^{-0.7}$ power law and with the Calzetti curve. Conroy (2010) found no evidence of the presence of a UV bump using the $B-R$ color of star-forming galaxies at $0.6 < z < 1.4$.

However, there is ample evidence of the presence of a UV bump at 2175 Å, although not as strong as for the MW, not only in nearby, but also in high-redshift star-forming galaxies. Variations in the attenuation curve have also been observed. Burgarella et al. (2005) claimed that their UV- and FIR-selected galaxy samples have attenuation curves with a UV bump. Noll & Pierini (2005) and Noll et al. (2007, 2009a) also found strong evidence of a UV bump of moderate strength in one third of a sample of massive star-forming galaxies at $1 < z < 2.5$. By analyzing UV and optical colors of disk-dominated galaxies at $0.01 < z < 0.05$, Conroy et al. (2010) speculated that a strong UV bump could be present in their extinction curves. Wild et al. (2011) found evidence of the presence of a UV bump in local star-forming galaxies. Buat et al. (2011, 2012) used a modified Calzetti curve, which was originally proposed by Noll et al. (2009b) to allow for variation in the UV bump strength and the attenuation curve slope, for galaxies at $1 < z < 2.2$ and found evidence of a UV bump with a strength of ∼35% of the bump in the MW. They also showed that the resulting attenuation curves are on average slightly steeper than the Calzetti curve. Kriek & Conroy (2013) also applied the modified Calzetti curve to composite SEDs constructed from a survey of $0.5 < z < 2.0$ galaxies and found not only evidence of the presence of a UV bump, but also a strong correlation between the attenuation curve slope and the UV bump strength (see also Kriek et al. 2011). Shivaei et al. (2015) found that an attenuation curve steeper than the Calzetti curve is needed to reproduce the observed IR/UV ratios of galaxies younger than 100 Myr. Reddy et al. (2015) analyzed the dust attenuation curve of $z = 1.4$–2.6 galaxies and found marginal evidence of excess absorption at 2175 Å. High-redshift galaxies at $z = 2$–6.5, for which the UV and optical SEDs are dominated by OB stars, were also shown to have a clear UV bump feature (Scoville et al. 2015). Zeimann et al. (2015) found that the average attenuation curve in a sample of high-redshift ($1.90 < z < 2.35$) galaxies is similar to the Calzetti curve. However, it was also found that the attenuation curve slope at UV is shallower over the galaxy mass range $7.2 \lesssim \log M/M_\odot \lesssim 10.2$ and the UV slope steepens as the galaxy mass increases. Salmon et al. (2016) analyzed a sample of IR-luminous galaxies at $z \sim 1.5$–3 using a Bayesian analysis and found considerable diversity in the attenuation curves; galaxies with high color excess have shallower attenuation curves, and those with low color excess have steeper attenuation curves.

Interestingly, it was also demonstrated that adding a UV bump to the Calzetti curve significantly improves the agreement between photometric and spectroscopic redshifts at least for some galaxies (Massarotti et al. 2001; Ilbert et al. 2009). Detailed analyses of individual galaxies also revealed the presence of a UV bump. The UV-to-NIR SED of the central region of the M33 nucleus was found to be consistent with MW-type dust with a strong UV bump (Gordon et al. 1999a). Hoversten et al. (2011) analyzed medium-band UV photometry from the *Swift* UV/Optical Telescope (UVOT) and found evidence of a prominent UV bump in star-forming regions of M81 and Holmberg IX. Hagen et al. (2015) used *Swift* UVOT to measure the attenuation curve for star-forming regions in the SMC and M33 and found that both the slope of the curve and the strength of the 2175 Å bump vary across both galaxies.

An interesting technique to measure the attenuation properties of galaxies was used for a few cases of partially overlapping galaxy pairs (Holwerda & Keel 2013; Holwerda et al. 2013). In the technique, a foreground spiral is backlit by a more distant galaxy, and the spectra measured in overlapped parts are compared to those in non-overlapped parts to obtain the spatially resolved attenuation curves of the foreground galaxy. At optical wavelengths, the resulting attenuation curves were found to be generally gray, and the grayness was attributed to the mixing effect of a wide range of clumpy dust optical depth even in individual pixels (Holwerda & Keel 2013; Holwerda et al. 2013).

In understanding these observational results, radiative transfer studies play an essential role. The main question in these studies would be whether the differences between the attenuation curves for starburst and/or normal star-forming galaxies and the MW extinction curve are caused by intrinsic differences in dust properties or can be explained by radiative transfer effects. Gordon et al. (1997) and Witt & Gordon (2000) performed Monte Carlo radiative transfer calculations by assuming three geometrical configurations, filled with either homogeneous or two-phase clumpy density distributions, and two types of interstellar dust properties similar to those of the MW and the SMC. Their models reproduced not only the absence of a UV bump, but also the overall shape of the Calzetti attenuation curve, provided that one adopts the SMC-type dust and a clumpy shell-type dust distribution surrounding the starbursts. They also argued that the absence of a 2175 Å absorption feature in the Calzetti curve can only be explained with dust that lacks the 2175 Å feature in its extinction curve. It was also noted that there is no unique attenuation curve. By adopting a dusty foreground screen with a lognormal density distribution and the MW extinction curve, Fischera et al. (2003) and Fischera & Dopita (2005) provided a physical explanation on the shallow shape of the Calzetti curve. Later, Fischera & Dopita (2011) explained the lack of a 2175 Å bump by assuming that below a certain critical column density the UV bump carriers are destroyed by strong radiation fields.

In contrast, Granato et al. (2000) and Panuzzo et al. (2007) claimed that the lack of a UV bump in the Calzetti curve is caused by the age-dependent extinction in which newly formed young stars are strongly attenuated by dense molecular clouds, while old stars are less attenuated by the diffuse ISM. Inoue (2005) solved the radiative transfer equation with multiple anisotropic scattering through the clumpy ISM by using the "mega-grain" approximation, treating clumps as large dust grains, but with the effective absorption and scattering coefficients calculated from the properties of the dust of which

the clumps are composed. He found that the age-dependent attenuation gives rise to a much steeper attenuation curve for normal star-forming galaxies than the Calzetti curve. The Calzetti curve was interpreted by Inoue (2005) as a special case at high optical depth. We note, however, that his attenuation curves at high optical depth obtained using the MW extinction curve still show the UV bump, while those calculated using the SMC extinction curve are consistent with the Calzetti curve. Pierini et al. (2004) found that for highly inclined, weak bulge galaxies the 2175 Å feature was very weak in the global attenuation curves.

The theoretical models have supplied useful insights into the attenuation curves in star-forming and starburst galaxies. However, the origin of variations in the observed attenuation curve, such as found in Kriek & Conroy (2013), is still poorly understood. It is also not well known which processes determine the strength of the UV bump. In this paper, we therefore aim to define the primary determinant that shapes the attenuation curve. The present study is based on radiative transfer calculations that employ dust density distributions appropriate for a turbulent ISM. In Section 2 we present a description of the dust density model and the radiative transfer model. The main results are presented in Section 3, in which we describe the radiative transfer effects needed to understand the attenuation curve, and show that the wavelength dependence of the absorption efficiency (hereafter, absorption curve) is the most important factor in determining the shape of the attenuation curve. Our results are then compared with a strong correlation between the attenuation curve slope and the UV bump strength found by Kriek & Conroy (2013) and with a correlation between the slope and the $E(B-V)$ color excess found by Salmon et al. (2016). Radiative transfer models in which starlight originates only from locally dense regions are also briefly described. In Section 4 we consider the correlation of the observed attenuation curves with galaxy properties. We also discuss the UV bump-less attenuation curve in scattering-dominant geometry and report an indication of a weak UV bump feature in local starburst galaxies. The results are summarized in Section 5.

2. MODEL

2.1. Turbulent Medium

We first present a brief introduction to the ISM density distribution and then detail the algorithm that is employed to simulate the density structure in this study. The ISM is known to be clumpy and turbulent, with a hierarchical density structure that is often treated as scale-free, and/or fractal (e.g., Elmegreen & Scalo 2004). To represent a clumpy medium, a two- or multiphase medium has been adopted in some radiative transfer models (Witt & Gordon 1996, 2000; Witt et al. 1997; Bianchi et al. 2000; Seon & Witt 2012; Stalevski et al. 2012). However, these models ignored the hierarchical structure of the ISM. Elmegreen (1997) proposed a more complex algorithm to mimic hierarchically clumped clouds, which has been used for radiative transfer models in the dusty or photoionized ISM (Mathis et al. 2002; Barnes et al. 2015). However, this model also has a critical limitation that results in a large number of unrealistic empty holes.

The density field in the turbulent ISM can be represented by a power spectral density (PSD) in the Fourier domain and a probability density function (PDF) in real space. The PSDs of turbulent media are well represented by a power-law function in the inertial range over which viscous effects are not important (e.g., Padoan et al. 2004; Kim & Ryu 2005; Kritsuk et al. 2006). The PDFs of the three-dimensional (3D) density of the turbulent ISM are known to be close to lognormal in both numerical simulations and observations (Vazquez-Semadeni 1994; Padoan et al. 1997; Klessen 2000; Ostriker et al. 2001; Berkhuijsen & Fletcher 2008; Lombardi et al. 2008; Seon 2009; Froebrich & Rowles 2010; Seon et al. 2011; Burkhart & Lazarian 2012; Seon 2013; Berkhuijsen et al. 2015). Therefore, the statistical properties of a density field in the turbulent ISM can be characterized by two parameters: a standard deviation ($\sigma_{\ln\rho}$) of the logarithm of the density, and a power-law index (γ) of the density power spectrum (Seon 2012).

The two parameters should be related to the sonic Mach number $M_{\rm s}$ of the turbulent ISM. Seon (2009) combined numerical simulation results of Padoan et al. (2004), Kim & Ryu (2005), and Kritsuk et al. (2006), finding a relationship between $M_{\rm s}$ and γ,

$$\gamma = 3.81 M_{\rm s}^{-0.16}, \tag{1}$$

which is applicable to isothermal hydrodynamic turbulence. In the isothermal hydrodynamic regimes, the variance of the log-density is found to be related to $M_{\rm s}$ according to

$$\sigma_{\ln\rho}^2 = \ln(1 + b^2 M_{\rm s}^2), \tag{2}$$

where the proportional constant b is $\sim$0.4 for natural turbulence forcing mode (e.g., Federrath et al. 2008, 2010). More complex relations between the density variance and Mach number have been proposed for isothermal magnetized gas or for the ISM in the non-isothermal regime (Molina et al. 2012; Nolan et al. 2015). However, the simple relation in Equation (2) is sufficient for the present purpose, which is to pursue the general properties of radiative transfer effects. Given a Mach number, the standard deviation and power spectral index of the lognormal density are determined by the above two equations.

A Gaussian random field $\rho_g(\boldsymbol{x})$ for a given power-law index γ_g is generated by first assigning 3D Fourier coefficients $s(\boldsymbol{k}) = |s(\boldsymbol{k})|\, e^{i\phi(\boldsymbol{k})}$ of $\rho_g(\boldsymbol{x})$ defined over the 3D wavenumber grid $\boldsymbol{k} = (k_x, k_y, k_z)$ using a prescription similar to those described in Stutzki et al. (1998) and Elmegreen (2002). The Fourier coefficients $s(\boldsymbol{k})$ are related to the random field $\rho_g(\boldsymbol{x})$ by

$$\rho_g(n_x, n_y, n_z) = \sum_{k_x=0}^{N_x-1}\sum_{k_y=0}^{N_y-1}\sum_{k_z=0}^{N_z-1} e^{2\pi i k_x n_x/N_x} e^{2\pi i k_y n_y/N_y} e^{2\pi i k_z n_z/N_z} \times s(k_x, k_y, k_z), \tag{3}$$

where N_x, N_y, and N_z are numbers of elements in each dimension, and (n_x, n_y, n_z) and (k_x, k_y, k_z) are indexes in real space and wavenumber space, respectively, ranging from 0 to $N_x - 1$, $N_y - 1$, and $N_z - 1$. The amplitudes $|s(\boldsymbol{k})|$ are taken to be Gaussian random variables with zero mean and a variance of $|\boldsymbol{k}|^{-\gamma_g}$. The mean value of zero in $\rho_g(\boldsymbol{x})$ is achieved by setting $s(0, 0, 0) = 0$. To obtain unit dispersion, the amplitudes are normalized by the sum $\sum_{\boldsymbol{k}} |s(\boldsymbol{k})|^2$ over the wavenumber grid. The phases $\phi(\boldsymbol{k})$ are randomly selected in the range of 0 to 2π. Because the density field should be real valued, the Fourier

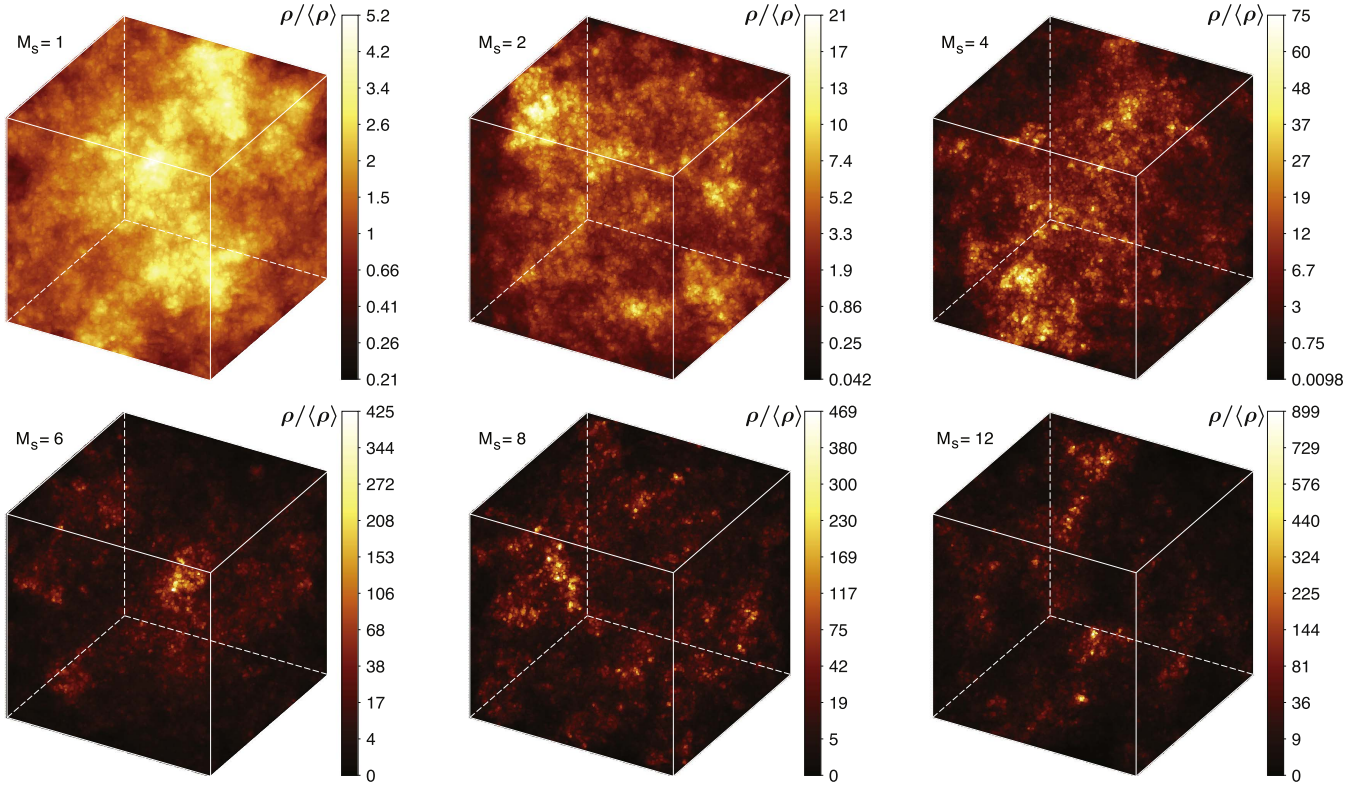

Figure 1. Some realizations of lognormal density fields for sonic Mach numbers $M_s = 1$, 2, 4, 6, 8, and 12. The color bars show $\rho/\langle\rho\rangle$, where $\langle\rho\rangle$ is the mean density.

coefficients must satisfy $s(\boldsymbol{k}) = s^*(-\boldsymbol{k})$. This results in the condition for the phases to be odd: $\phi(\boldsymbol{k}) = -\phi(-\boldsymbol{k})$, which can be easily realized by first generating a set of phases $\chi(\boldsymbol{k})$ and then taking $\phi(\boldsymbol{k}) = \chi(\boldsymbol{k}) - \chi(-\boldsymbol{k})$. The real space counterparts are then calculated using the fast Fourier transform library FFTW (Frigo & Johnson 2005); the resulting density field $\rho_g(\boldsymbol{x})$ is a Gaussian random field with zero mean and unit dispersion (Voss et al. 1988, pp. 21–70).

The Gaussian random field is multiplied by the standard deviation $\sigma_{\ln\rho}$ of the logarithmic density, exponentiated, and then multiplied by a normalization constant ρ_0 adjusted to yield a given mean density; this results in the lognormal density field $\rho(\boldsymbol{x}) = \rho_0 \exp[\sigma_{\ln\rho}\rho_g(\boldsymbol{x})]$. However, the power-law spectral index of the resulting lognormal density field (γ) is different from that of the input Gaussian field (γ_g). The relationship between the power spectral indexes of the lognormal density field and the Gaussian field was derived in Seon (2012). The power spectral index of $\rho(\boldsymbol{x})$ was obtained by least-squares fit over the range of $3 \leqslant |\boldsymbol{k}| \leqslant 35$. This relationship, together with Equations (1) and (2), was used to obtain a random realization of the lognormal density field with the spectral index γ and standard deviation $\sigma_{\ln\rho}$ appropriate for a given Mach number. In this way, 10 random realizations of the lognormal density distribution with box size of $N^3 = 128^3$ were generated for each Mach number of $M_s = 1$, 2, 4, 6, 8, 10, 12, 16, and 20. Some realizations of the lognormal density field are shown in Figure 1. Because of the lognormal property of the density fields, high-density cells are mostly contained in a relatively small fraction of the volume. Figure 2 shows variations of the fraction of volume $f_{\rm volume}$ occupied by a mass fraction $f_{\rm mass}$, when the mass fraction is measured from the lowest density cell, for each Mach number. The results

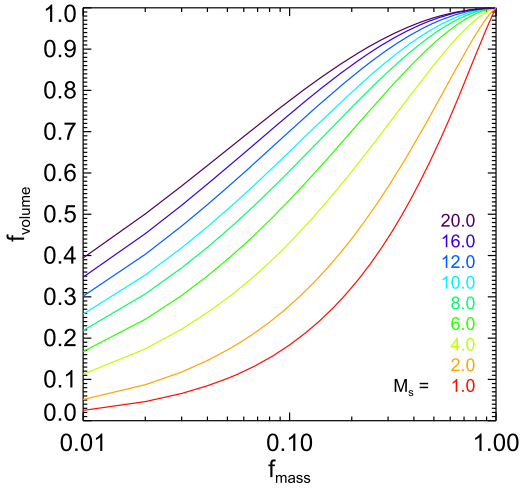

Figure 2. Volume fraction vs. mass fraction for the density fields with Mach numbers of $M_s = 1$, 2, 4, 6, 8, 10, 12, 16, and 20.

presented here are results averaged over the 10 realizations for each Mach number.

2.2. Dust Extinction Curves

To examine which type of underlying dust model best reproduces the Calzetti attenuation curve and other attenuation curves inferred from star-forming galaxies, five dust types are considered: three theoretical dust models adopted from Weingartner & Draine (2001) and Draine (2003) for the MW, LMC, and SMC bar, and two empirical models for the MW and SMC from Witt & Gordon (2000). The dust models of Weingartner & Draine (2001) are referred to as MW-WD, LMC-WD, and SMC-WD, and the dust models of Witt &

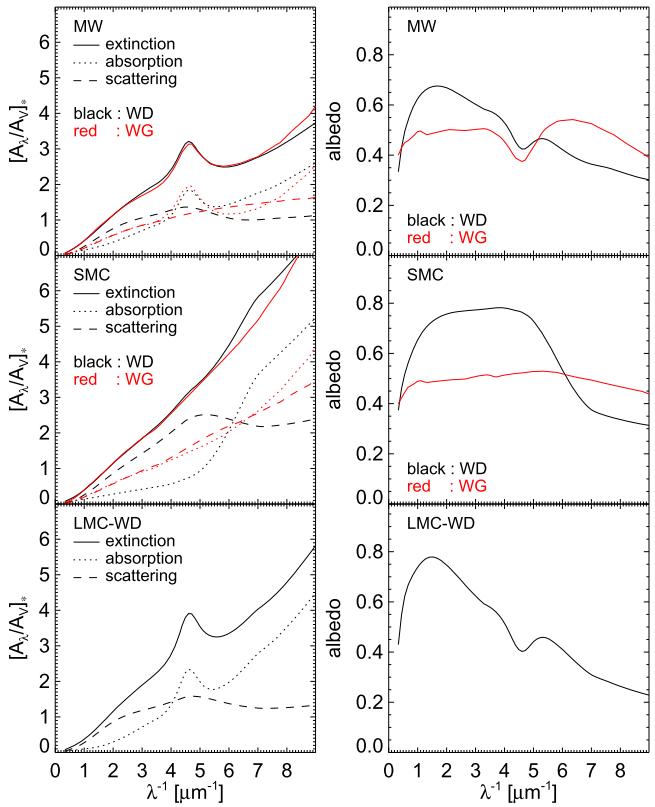

Figure 3. Comparison of the extinction and albedo curves of Weingartner & Draine (2001) and Witt & Gordon (2000). In the left panels, the extinction, absorption, and scattering curves are denoted as solid, dotted, and dashed lines, respectively. In the top and middle panels, the MW and SMC curves of Weingartner & Draine (2001) and Witt & Gordon (2000) are denoted as black and red lines, respectively. The LMC curves of Weingartner & Draine (2001) are also shown in the bottom panels.

Gordon (2000) are referred to as MW-WG and SMC-WG. As we discuss later, the resulting attenuation curve primarily depends on the underlying absorption curve (wavelength dependence of absorption) rather than on the extinction (absorption+scattering) curve. The wavelength dependences of albedo (a) and scattering phase function asymmetry factor (g) were calculated using the Mie theory and the size distributions of carbonaceous and silicate grain populations obtained in Weingartner & Draine (2001). It should be noted that the albedo and scattering phase factor for the MW-WG dust were empirically determined based on the observations of reflection nebulae, which usually have higher values of $R_V = A_V/E(B-V)$ than 3.1. The scattering phase function for the SMC-WG dust is the same as that of the MW-WG dust. The albedo for the SMC-WG dust was obtained by modifying that of the MW-WG to reflect the lack of a 2175 Å absorption bump in the SMC extinction curve.

Figure 3 compares the wavelength dependences of extinction, absorption, and scattering cross-sections normalized by the extinction values at V band for the MW- and SMC-type dusts of Weingartner & Draine (2001) and Witt & Gordon (2000). The extinction, absorption, and scattering cross-sections for the LMC-type dust of Weingartner & Draine (2001) are also shown in the bottom panels. The albedos of the MW-WG and SMC-WG dust types remain more or less constant except for the absorption feature at ~2175 Å in the MW-WG dust. However, the albedo of the MW-WD dust gradually decreases at $\lambda^{-1} > 1.5\,\mu\mathrm{m}^{-1}$ and that of the SMC-WD dust decreases at $\lambda^{-1} > 5\,\mu\mathrm{m}^{-1}$. This results in a gradual decrease of the scattering cross section of the MW-WD dust at $\lambda^{-1} > 4.5\,\mu\mathrm{m}^{-1}$; in contrast, the scattering cross section of the MW-WG dust gradually increases as wavelength decreases. Similar trends are also found for the SMC-type dust models. These properties are further discussed with respect to the fraction of scattered light in Section 3.1.

2.3. Radiative Transfer Code

For the radiative transfer simulation in turbulent media with lognormal density distributions, the 3D Monte Carlo radiative transfer code MoCafe (Monte Carlo radiative transfer) was used (Seon et al. 2014; Seon 2015). The basic Monte Carlo radiative transfer algorithms have been detailed by many authors (Gordon et al. 2001; Baes et al. 2011; Steinacker et al. 2013). Here, the main techniques implemented in the code are briefly described. The forced first scattering technique was adopted for efficiency at low optical depths, as in most Monte Carlo radiative transfer codes (Cashwell & Everett 1959). A forced scattering technique, as implemented in Baes et al. (2011), in which photon packets are always forced to be scattered until the weight of the photon packet decreases to a minimum value, was also implemented and confirmed to yield results that are consistent with the forced first scattering technique. At high optical depths, the scattering scheme of Baes et al. (2011) is faster, but underestimates the output flux unless a sufficiently small minimum weight is adopted. The scheme of Baes et al. (2011) adopting a very small minimum weight is in fact equivalent to the forced first scattering scheme in speed.

MoCafe employs a fast voxel traversal algorithm for ray tracing, developed for computer graphics rendering by Amanatides & Woo (1987). The voxel traversal algorithm dramatically increases the speed of radiative transfer calculation compared to the conventional methods of Wolf et al. (1999) or Kurosawa & Hillier (2001). The algorithm also provides a method to accurately track the paths of photon packets, which is crucial for simulations in highly inhomogeneous media, even with single precision floating-point numbers. The code uses the KISS (keep it simple, stupid) random number generator of Marsaglia & Zaman (1993), which is up to about five times faster and has a much longer period than the popular "ran2" generator given in Press et al. (1992). A new fast algorithm to accelerate the simulation at high optical depths was also developed. The algorithm is based on the path length stretching technique combined with photon splitting to minimize the fluctuation of photon weight. This is similar to the composite path length stretching algorithm of Baes et al. (2016). More details will be published in a separate paper.

Radiative transfer calculations were performed for 44 wavelengths defined in a wavelength range of $\lambda^{-1} = 0.3$–$8.9\,\mu\mathrm{m}^{-1}$ with a bin size of $\Delta\lambda^{-1} = 0.2\,\mu\mathrm{m}^{-1}$. The wavelength of a photon packet is selected among the wavelengths so that the input SED is constant. The number of photon packages for each wavelength was varied between 10^5 and 10^7 depending on the optical depth of the system. Photon packages leaving the system were recorded for the output SED f_λ^{esc} as a function of wavelength. The attenuation optical depth as a function of wavelength is then calculated by

$$\tau_\lambda^{\mathrm{att}} = -\ln(f_\lambda^{\mathrm{esc}}). \quad (4)$$

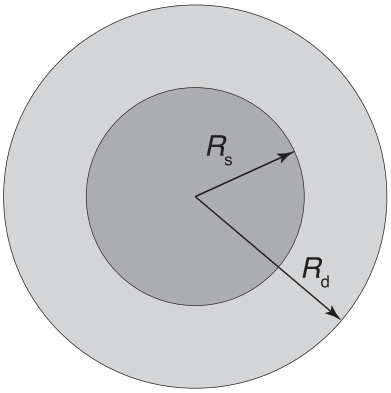

Figure 4. Geometry used in the present study. R_s and R_d represent the radii of the stellar and dust distributions, respectively.

The attenuation optical depth is always smaller than the extinction optical depth, which is defined by the center-to-edge optical depth of a cloud, because the dust albedo is always nonzero and the stars are distributed throughout the extended volume. Total attenuation at a wavelength λ is defined by $A_\lambda = (2.5\log_{10}e)\tau_\lambda^{\rm att} = 1.086\tau_\lambda^{\rm att}$ as analogous to the total extinction. Attenuation color excess $E(B-V)$ is defined by $A_B - A_V$ as for the extinction color excess. In this paper, extinction-related quantities are denoted inside the square brackets $[]_*$ with an asterisk to distinguish them from those for attenuation; for instance, the total extinction is denoted by $[A_\lambda]_*$.

Scattering directions of photons were randomly determined to follow a numerical phase function calculated by the Mie theory for the dust models of Weingartner & Draine (2001) or a Henyey-Greenstein phase function, using the algorithm of Witt (1977), for the dust models of Witt & Gordon (2000), who do not provide a size distribution of dust grains.

2.4. Geometry

In the present study, both the turbulent dusty medium and the stellar sources were assumed to be spherically distributed; radii for stellar and dust distributions are defined by R_s and R_d, respectively, as shown in Figure 4. Although the dust distribution is highly inhomogeneous, photon sources were uniformly distributed within the sphere, unless otherwise specified. The dust density was set to zero for $r > R_d$. The radial extents of the stellar source were varied within a range of $0 \leqslant R_s/R_d \leqslant 1$; the case of $R_s = 0$ represents a compact OB association surrounded by a cloud, while the case of $R_s/R_d = 1$ corresponds to the "dusty" configuration of Witt & Gordon (2000) in which photon sources are uniformly distributed over the spherical dusty medium.

The optical depth of the medium is measured from the center to the cloud surface at the V-band wavelength ($\lambda = 0.55\ \mu$m). As in Witt & Gordon (2000), the homogeneous radial optical depth τ_V at V band for a lognormal density cloud is defined by the center-to-edge optical depth of a cloud with a constant density and radius R_d, but with the same dust mass as the lognormal density cloud. For each Mach number, τ_V was varied from 0.1 to 20. To compare with the results of Witt & Gordon (2000), radiative transfer calculations were also performed for the clumpy, "shell" geometry, in which stars are distributed only within $R_s/R_d \leqslant 0.3$, while dust grains are only located outside of the stellar distribution radius. Ten realizations of the clumpy density distribution according to Witt & Gordon (2000) were produced, and the radiative transfer calculations were averaged to remove any possible peculiarity due to a specific realization, as for the case of the turbulent density distribution. The results presented in this paper are averages over all directions.

3. RESULTS

3.1. Radiative Transfer Effects

In dealing with an extinction toward a point source, the amount of total extinction $[A_\lambda]_*$ at a wavelength λ as well as the color excess $[E(B-V)]_* \equiv [A_B - A_V]_*$ are linearly proportional to the dust column density (or to the optical depth at a particular wavelength) unless the physical properties of dust grains are changed; thus, the total-to-selective extinction $[R_V]_* \equiv [A_V/E(B-V)]_*$ remains constant as optical depth varies. However, for spatially extended sources, the linearity of the total attenuation A_λ, defined analogously to the total extinction, on the amount of dust is no longer valid even in a uniform medium (Witt et al. 1992b; Witt & Gordon 2000). Consequently, the color excess $E(B-V)$ is a nonlinear function of A_V; the total-to-selective attenuation R_V is also not a constant.

The first and second columns of Figure 5 show A_V and $E(B-V)$, respectively, calculated as a function of the homogeneous radial optical depth τ_V for the MW-WD, LMC-WD, and SMC-WD dust types. The total attenuation A_V and color excess $E(B-V)$ decrease as the Mach number and/or the stellar distribution size increases for a given τ_V. The MW-WD model shows the highest total attenuation A_V for a given R_s/R_d, τ_V, and M_s, whereas the color excess $E(B-V)$ is highest for the LMC-WD model. The total attenuation and color excess are both increasing functions of the homogeneous optical depth τ_V. However, the increase rapidly slows down. Especially at high Mach number ($M_s \gtrsim 6$) and for extended stellar distribution ($R_s/R_d \gtrsim 0.8$), $E(B-V)$ starts to saturate at $\tau_V \sim 5$, indicating that the actual amount of dust cannot be determined by the color excess measurement. For $M_s \gtrsim 6$ and $R_s/R_d \gtrsim 0.8$, $E(B-V) \lesssim 0.4$ for the MW-WD model. As noted in Witt & Gordon (2000), $E(B-V)$ of LBGs crowds around values of $\sim$0.2, rarely exceeding 0.4 (Sawicki & Yee 1998; Steidel et al. 1999; Shapley et al. 2001; Reddy et al. 2008). The results in Figure 5 suggest that the LBGs are highly turbulent or clumpy with stars that are spatially mixed well with dust. As we show in the next section, the saturation of $E(B-V)$ is accompanied by an attenuation curve that is grayer or shallower than the underlying extinction curve.

Variation of R_V is also shown as a function of A_V and $E(B-V)$ in the third and fourth columns of Figure 5. In general, R_V increases with increase of M_s, R_s/R_d and τ_V. The ratio R_V monotonically increases with A_V except for the SMC-WD models with low M_s values, in which R_V decreases to a minimum at $A_V \sim 0.6$ and then increases monotonically. For the models with high R_s/R_d values, R_V is not well constrained as a function of $E(B-V)$ because of the saturation of $E(B-V)$. This also indicates that the absolute amount of dust is not well determined by the color excess $E(B-V)$.

The saturation in $E(B-V)$ is due to three reasons: (1) dust density distribution, (2) scattering and (3) free escape of starlight through relatively low column density paths. The

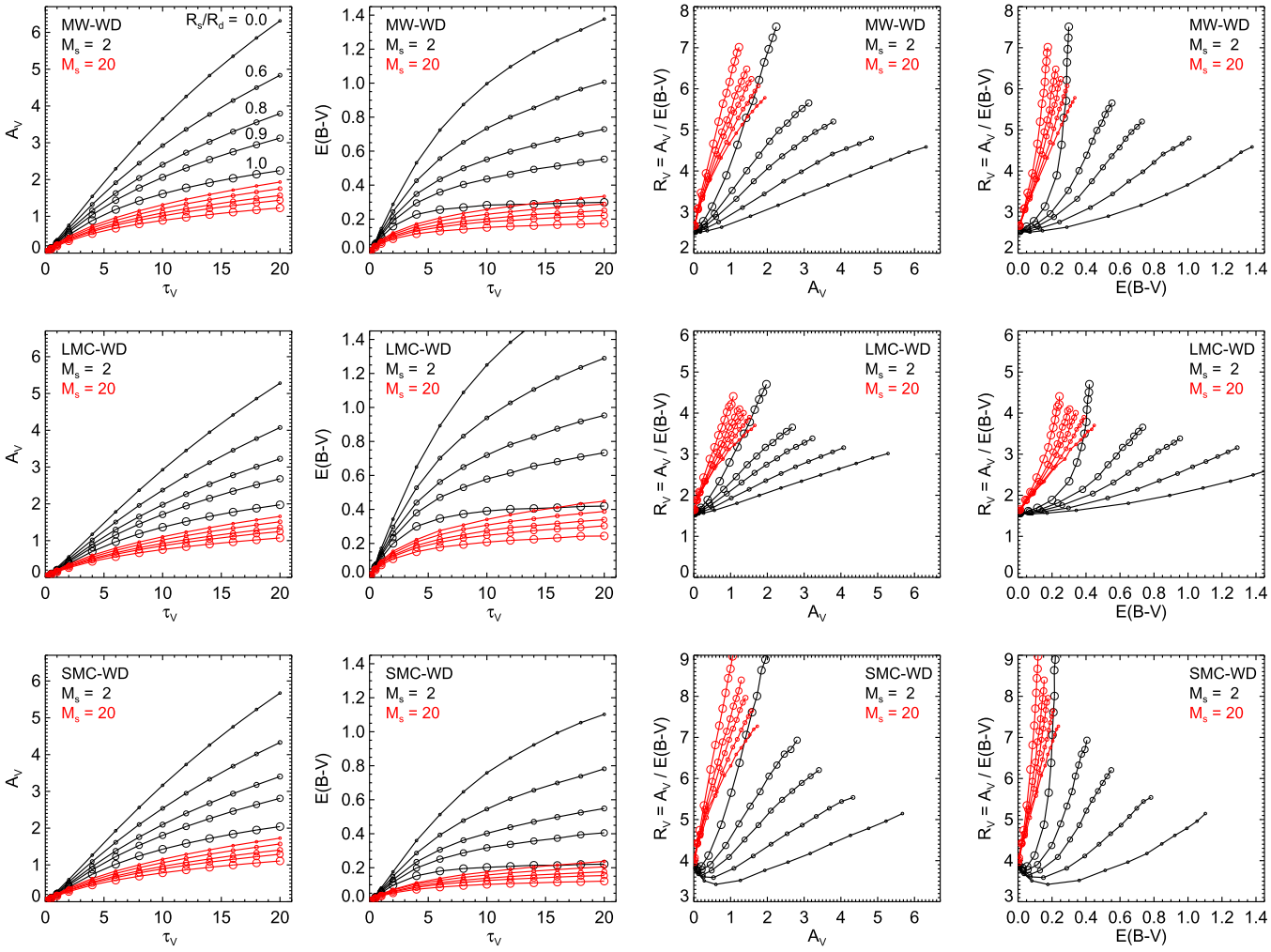

Figure 5. First and second columns: attenuation A_V and color excess $E(B-V)$ as a function of homogeneous optical depth τ_V. Total-to-selective attenuation R_V as a function of A_V. Fourth column: R_V as a function of the $E(B-V)$ color excess. First, second, and third rows represent the results obtained for the MW, LMC, and SMC dust types of Weingartner & Draine (2001), respectively. The homogeneous optical depth τ_V increases from 0.1 up to 20. Symbol size is proportional to the size of stellar distribution, corresponding to $R_s/R_d = 0.0$, 0.6, 0.8, 0.9, and 1.0. Black and red denote the sonic Mach numbers of $M_s = 2$ and 20, respectively.

saturation of $E(B-V)$ indicates that $E(B-V)$ is not a good proxy to accurately measure dust attenuation (Witt & Gordon 2000); even a small measurement error in $E(B-V)$ would give rise to a large error in attenuation.

We also note that scattered light partially compensates for extinction—the integrated light consists of scattered light and direct starlight. Figure 6 shows the SEDs of scattered light relative to total light for various models with the MW and SMC dust types. The fraction of scattered light depends on dust scattering properties, wavelength, star/dust geometry, and on the total dust column density. Multiple scattering becomes increasingly important as τ_V increases while the direct starlight decreases; hence, the fraction of scattered light increases with τ_V, as shown in the first column of Figure 6. For the parameters ($M_s = 2$ and $R_s/R_d = 0.8$) in column one, scattered light dominates the output SEDs at $\tau_V \gtrsim 2$. The multiple scattering effect becomes less important with increasing M_s and R_s/R_d, as shown in the second and third columns of Figure 6. As M_s increases, the density contrast between high- and low-density cells and the volume-filling fraction of low-density cells both increase. This allows more starlight to escape relatively easily. For large source distributions (higher R_s/R_d), photons originating from locations close to the boundary can also escape freely. Thus, the fraction of scattered light anticorrelates with M_s and R_s/R_d.

It has been known that the scattered light is relatively "bluer" than direct starlight and thus partially compensates for reddening by extinction (Witt et al. 1992b; Witt & Gordon 2000). However, the "blueing" effect of scattered light is true only in optical and NIR wavelengths ($\lambda^{-1} \lesssim 2.5$ μm^{-1}). At UV wavelengths ($\lambda^{-1} \gtrsim 2.5$ μm^{-1}), scattered light can be either bluer or redder than direct starlight, depending on the adopted dust type, as shown in Figure 6. For the two dust types of Witt & Gordon (2000), scattered light is bluer than direct starlight in most of the wavelength range except at $\lambda^{-1} \gtrsim 7\,\mu m^{-1}$ in the MW-WG dust models. On the other hand, scattered light is redder at $\lambda^{-1} \gtrsim 2\,\mu m^{-1}$ for the MW-WD dust and at $\lambda^{-1} \gtrsim 5\,\mu m^{-1}$ for the SMC-WD dust; therefore, scattering gives a reddening effect at UV wavelengths for the MW-WD and SMC-WD dust types. A "reddening" or "blueing" effect similar to that for the MW-WD dust type was also found for the LMC-WD dust type.

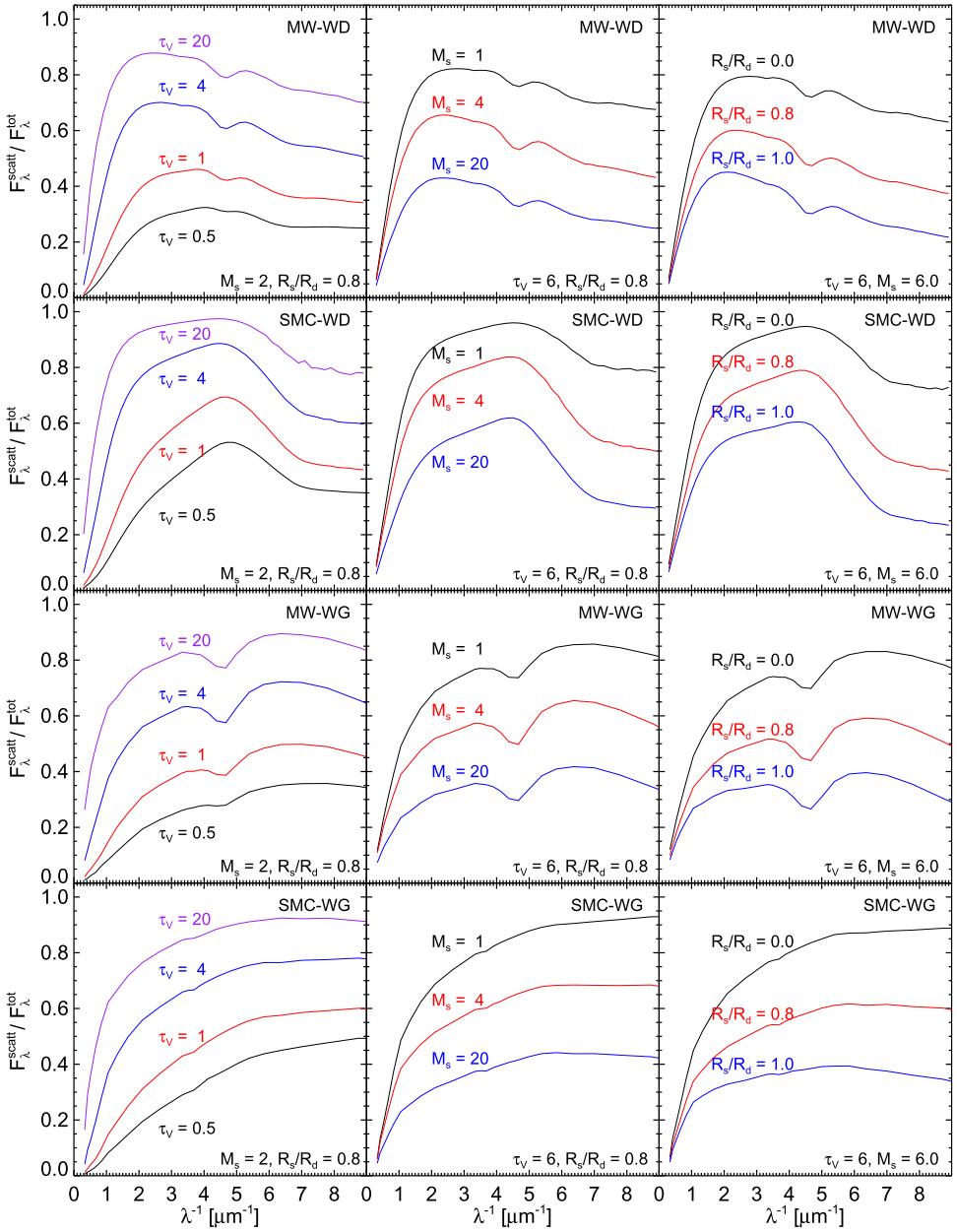

Figure 6. Fraction of scattered light. The left, middle, and right columns show variations of the relative SEDs as optical depth, Mach number, and stellar distribution size vary. The first and second rows were calculated with the MW- and SMC-type extinction curves of Weingartner & Draine (2001), respectively. The third and fourth rows were calculated assuming the MW- and SMC-type extinction curves of Witt & Gordon (2000), respectively.

The reddening or blueing effect of scattering can be understood by examining the wavelength dependence of the albedo of each dust type shown in Figure 3. From the figure, it can be immediately recognized that the shape of the normalized SED of scattered light is mainly determined, especially at short wavelengths, by the wavelength dependence of the albedo. At the longest wavelengths ($\lambda^{-1} < 1\,\mu\mathrm{m}^{-1}$), starlight escapes relatively freely from the dusty media because of the low optical depth. Therefore, the scattered fraction is relatively low and approximately proportional to the optical depth. The increase in optical depth with λ^{-1} gives rise to a gradual increase in the scattered fraction with λ^{-1}. However, as λ^{-1} further increases, the optical depth becomes much larger than unity and most of the total output SED originates near the surface of the last scattering; thus, the fraction of scattered light is roughly proportional to the albedo, and the shape of the normalized SED of scattered light resembles the albedo curve at shorter wavelengths. As τ_V is increased, the overall shape of the normalized SED of the scattered light becomes closer to the albedo curve. For models with $\tau_V \gtrsim 4$, the normalized SEDs of scattered light are very close to the albedo function at $\lambda^{-1} \gtrsim 2\,\mu\mathrm{m}^{-1}$; therefore, whether scattering yields either a reddening or a blueing effect at $\lambda^{-1} \gtrsim 2\,\mu\mathrm{m}^{-1}$ is primarily determined by the shape of the adopted albedo curve. In an observational study of the FUV ($5.7\ \mu\mathrm{m}^{-1} < \lambda^{-1} < 7.4\ \mu\mathrm{m}^{-1}$) continuum background, Seon et al. (2011) found that the scattered FUV continuum background is relatively redder than the direct stellar spectrum and attributed the result to the increase in scattering albedo with wavelength; therefore, the diffuse FUV background observation supports the wavelength dependence of the albedo of the MW-WD dust type. However, we note that scattering is more efficient at *B*-band wavelength

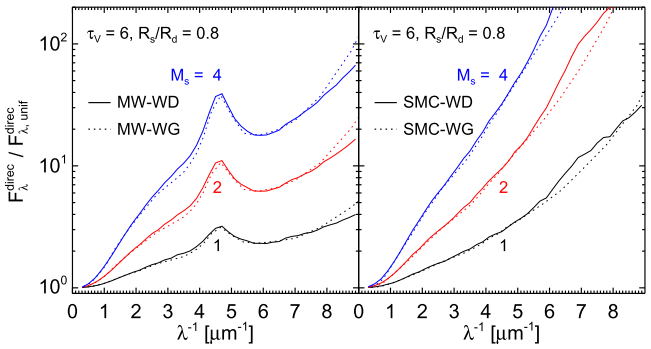

Figure 7. Ratio of direct starlight escaping from a clumpy medium ($F_\lambda^{\rm direc}$) to that from a uniform medium ($F_{\lambda,{\rm unif}}^{\rm direc}$). The relative SED is shown for $M_{\rm s}=1$ (black), 2 (red), and 4 (blue). The left and right panels were calculated with the MW- and SMC-type extinction curves, respectively. The dust types of Weingartner & Draine (2001) and Witt & Gordon (2000) are denoted as solid and dotted lines, respectively.

than at V-band wavelength for all of the dust types considered in the present study.

The saturation of $E(B-V)$ is also observed for higher Mach numbers (i.e., higher density contrasts) and/or more extended stellar distributions. As already noted, increase in $M_{\rm s}$ or $R_{\rm s}/R_{\rm d}$ for a given τ_V allows more direct starlight to escape freely without any interaction with dust grains. The middle and right columns of Figure 6 show the increase in direct starlight component with increasing $M_{\rm s}$ and $R_{\rm s}/R_{\rm d}$, respectively. The contribution of direct starlight not only causes $E(B-V)$ to saturate, but also makes the attenuation curves grayer.

The above three effects play complex roles in forming attenuation curves, which are in general grayer than the underlying extinction curve. Direct starlight escaping from a clumpy medium is bluer than that from a uniform medium (see Figure 7). This is because a clumpier medium yields a smaller effective optical depth and the effect becomes more important as optical depth increases with decreasing wavelength. In NIR and optical wavelengths, scattering provides an even stronger blueing effect in the output SED regardless of the dust type. However, at UV wavelengths, scattering can play an opposite role for some dust types (e.g., MW-WD or SMC-WD).

3.2. Attenuation Curves

Before we discuss attenuation curves, it is first noted that Calzetti et al. (1994) originally derived a selective attenuation curve relative to a zero-point at V band (0.55 μm) and normalized to $E(B-V)$, equivalent to $E(\lambda-V)/E(B-V)$, but not a total attenuation. Since they averaged spectra of sample galaxies at different distances and with different luminosities to derive an average attenuation curve for starburst galaxies, they had to arbitrarily impose a zero-point at a conventional wavelength, e.g., 0.55 μm. The zero-point was found to be $R_V=A_V/E(B-V)=4.88\pm0.98$ by comparing the attenuated stellar luminosity with the reprocessed FIR emission (Calzetti 1997). Later, the zero-point was revised to be $R_V=4.05\pm0.80$ in Calzetti et al. (2000), providing the final Calzetti curve in a piece-wise functional form of $A_\lambda/E(B-V)\equiv E(\lambda-V)/E(B-V)+R_V$.

Note that it was implicitly assumed that (1) $E(B-V)$ is a proxy for the dust attenuation and (2) R_V is independent of $E(B-V)$ in deriving the zero-point. However, for fixed dust properties the "observed" total-to color excess ratio R_V is no longer a constant, as shown in Figure 5. The ratio R_V increases with the optical depth, Mach number, and the source size. As noted in Witt & Gordon (2000), the attenuation curve of galaxies is not unique but shows large variations. This is because neither A_V nor $E(B-V)$ are linear functions of τ_V, and R_V is not a constant. The non-constancy of R_V may give an impression that a calculated $A_\lambda/E(B-V)$ curve is somewhat different from the Calzetti curve even when the $E(\lambda-V)/E(B-V)$ curve seems to agree well with that of Calzetti. It should also be noted that attenuation correction in fitting galactic SEDs is done by using a total attenuation curve A_λ normalized to a total attenuation value at a particular wavelength, such as A_λ/A_V (Noll et al. 2009b; Buat et al. 2011; Kriek & Conroy 2013) or A_λ/A_{1300} (Scoville et al. 2015). However, both the nonlinear relation between A_V and $E(B-V)$ and the non-constancy of R_V would also yield a large deviation of the calculated A_λ/A_V curves from that of Calzetti. As we discuss in Section 4.4, the variability in the attenuation curves for the local starburst galaxies is indeed significant.

We therefore compare the calculated attenuation curves in three different forms: $E(\lambda-V)/E(B-V)$, $A_\lambda/E(B-V)$, and A_λ/A_V. Figures 8–10 show the calculated attenuation curves as functions of inverse wavelength for the MW-WD, LMC-WD, and SMC-WD dust types, respectively. In each figure, results are shown for Mach numbers $M_{\rm s}=2$ and 20, and the stellar distribution size of $R_{\rm s}/R_{\rm d}=0.2$ and 1.0. In each panel of the figures, the homogeneous optical depth τ_V is varied from 1 to 20 and the variation is denoted in colors. The Calzetti curve is also shown in black for comparison. The upper and lower black curves in the $A_\lambda/E(B-V)$ and A_λ/A_V curves denote the uncertainty boundaries of the Calzetti curve estimated from the uncertainty range of $R_V=A_V/E(B-V)=4.05\pm0.80$, as derived in Calzetti et al. (2000). Note, however, that no error range in the $E(\lambda-V)/E(B-V)$ curve was provided in Calzetti et al. (2000).

In Figures 8–10, we first note that regardless of the adopted dust type, the attenuation curve becomes grayer as the homogeneous optical depth τ_V, the Mach number $M_{\rm s}$, and the size of the source distribution $R_{\rm s}/R_{\rm d}$ each increase. The shallow slopes shown in the models, especially with large optical depths, are attributable to both the turbulent density structure and scattering effects, as discussed in Section 3.1. The shape of the attenuation curve is least affected by varying $R_{\rm s}/R_{\rm d}$, compared to the effects that are due to changes of τ_V and $M_{\rm s}$; especially at the highest Mach number ($M_{\rm s}=20$), the variation of the curve that is due to the $R_{\rm s}/R_{\rm d}$ change is marginal. The largest variations of the curves are produced by changing τ_V. These trends are further discussed in Section 3.6. It is also noted that the shallower curves have weaker UV bump features. Similar trends have been found in Witt et al. (1992b) and Witt & Gordon (2000).

The most important result from the figures is that the MW-WD model calculations are in general consistent with the Calzetti curve *except* for the presence of a UV absorption feature. This is true especially for higher $M_{\rm s}$ and $R_{\rm s}/R_{\rm d}$. The $E(\lambda-V)/E(B-V)$ and A_λ/A_V curves averaged over a wide range of τ_V for each set of $M_{\rm s}$ and $R_{\rm s}/R_{\rm d}$ coincide well with the Calzetti curve, provided that $M_{\rm s}\gtrsim4$ or $R_{\rm s}/R_{\rm d}\gtrsim0.2$ *and* the UV bump is removed. We show later that the Calzetti attenuation curve is very well reproduced by MW-WD dust type with the UV bump component suppressed or entirely removed. Except for the UV bump, the average attenuation

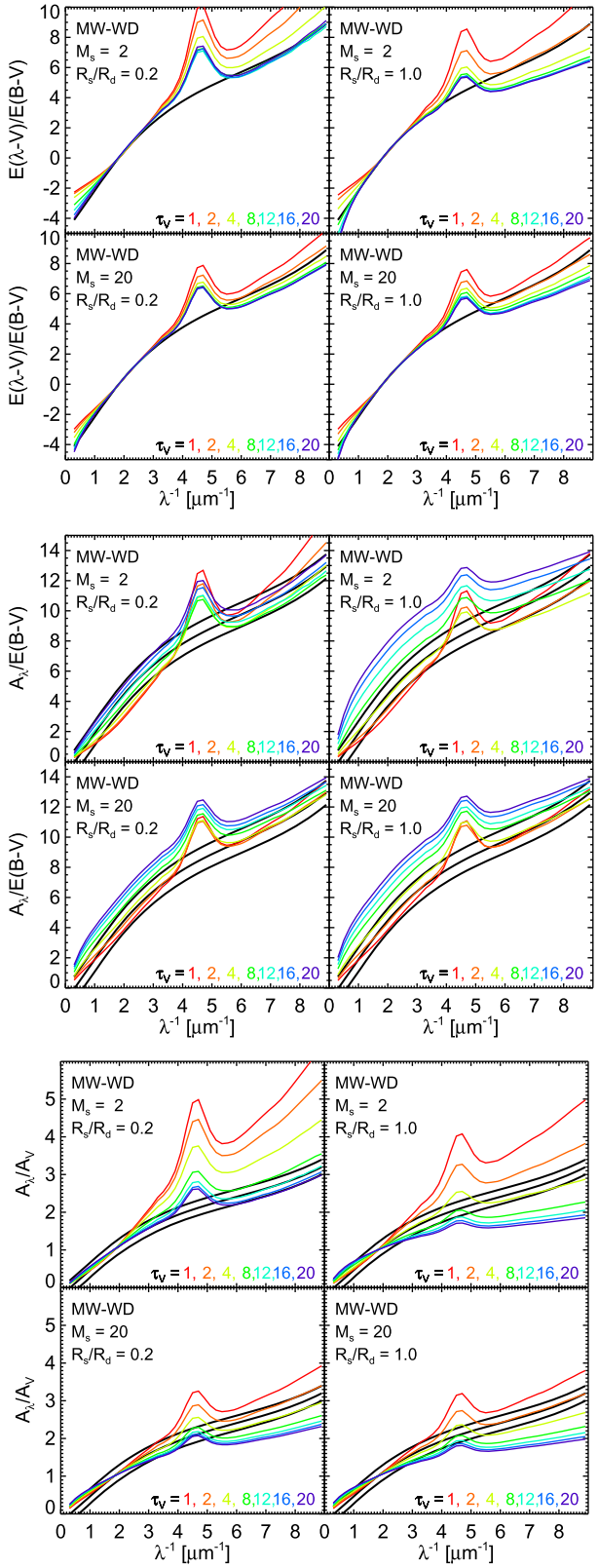

Figure 8. Attenuation curves for the MW dust of Weingartner & Draine (2001) are plotted in three forms: (top) $E(\lambda - V)/E(B - V)$, (middle) $A_\lambda/E(B - V)$, (bottom) and A_λ/A_V. The black curves denote the Calzetti curve and its uncertainty boundaries. The upper and lower bounds of the Calzetti curve in middle and bottom panels are obtained using the error range of R_V. Note that no uncertainties of the Calzetti curve in the $E(\lambda - V)/E(B - V)$ form (shown in the top panels) are provided.

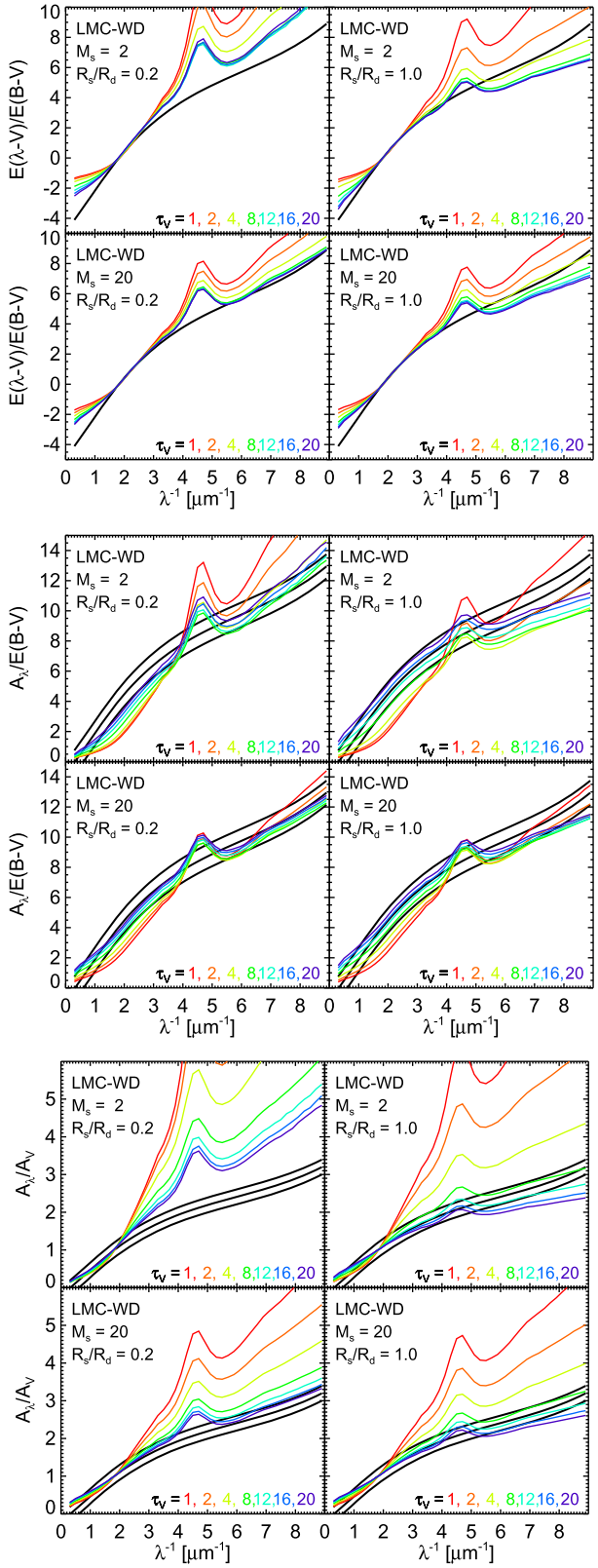

Figure 9. Attenuation curves for the LMC dust of Weingartner & Draine (2001) are plotted in three forms: (top) $E(\lambda - V)/E(B - V)$, (middle) $A_\lambda/E(B - V)$, (bottom) and A_λ/A_V. The black curves denote the Calzetti curve and its uncertainty boundaries.

curve for $R_s/R_d = 1$ and $\tau_V \sim 2$–4 is found to agree well with the Calzetti curve regardless of the Mach number. For low values of the parameters M_s, R_s/R_d, and τ_V, the attenuation curves appear to be slightly steeper than the Calzetti curve. On the other hand, the attenuation curves are relatively shallower at high values of τ_V. The total-to-selective attenuation ratio R_V for high values of M_s and R_s/R_d tends to be slightly higher than that of the Calzetti curve, as shown in the $A_\lambda/E(B-V)$ curves.

For the LMC-WD dust type, the overall shape of the $A_\lambda/E(B-V)$ curves, except for the UV bump feature, for $M_s = 20$, $\tau_V \gtrsim 4$ or $M_s = 2$, $\tau_V \gtrsim 16$ seem to agree with the Calzetti curve, while A_λ/A_V curves show much steeper slopes except for the highest optical depths ($\tau_V \gtrsim 8$) and the star/dust geometries with $R_s/R_d > 0.8$. The $E(\lambda-V)/E(B-V)$ curve at $\lambda^{-1} > \lambda_V^{-1}$ is also consistent with the Calzetti curve for high M_s and R_s/R_d values. We note that when we disregarded the UV bump, the calculated attenuation curves for the MW-WD dust were consistent with the Calzetti curve over a wide range of parameters, whereas the attenuation curves obtained with the LMC-WD dust agreed within a more limited parameter range. We also note that R_V is always lower for the LMC-WD dust than for the MW-WD dust, as shown in $A_\lambda/E(B-V)$ curves. In contrast to the MW-WD and LMC-WD dust types, the attenuation curves calculated with the SMC-WD dust are generally not consistent with the Calzetti curve in all three forms.

3.3. What Determines the Shape of Attenuation Curve?

The above result is in contrast to the conclusion of Witt & Gordon (2000), in which they claimed that SMC-type dust in a clumpy shell geometry can reproduce the Calzetti curve. In this section, we identify the primary cause of the discrepancy. The discrepancy must be due to differences in either the geometry/density distribution or in the wavelength dependence of albedo, or both. We have assumed a lognormal density distribution, while Witt & Gordon (2000) assumed a two-phase density model. Witt & Gordon (2000) assumed a shell geometry with stars extending from the center to 0.3 of the system radius and dust extending from 0.3 to 1 of the system radius. In the present study, on the other hand, stars were uniformly distributed within a radius of R_s. The albedo curves in the present study were calculated using the Mie scattering theory according to the carbonaceous and silicate dust grain models of Weingartner & Draine (2001) and Draine (2003), whereas Witt & Gordon (2000) adopted empirically determined albedo curves estimated from comparisons of observational data of reflection nebulae with radiative transfer models.

First, we examine the geometrical effects. Figure 11 shows the results obtained for the clumpy shell geometry of Witt & Gordon (2000), but adopting the three dust types of Weingartner & Draine (2001). The resulting attenuation curves for all three dust types are very similar to those calculated with the turbulent media with $R_s/R_d \sim 1$ shown in Figures 8–10. Therefore, the difference in the adopted geometry and density distribution is evidently not the main reason for the discrepancy. The other possibility would be differences in the albedo curves. Figures 12 and 13 show the attenuation curves calculated for MW-WG and SMC-WG dust when the turbulent density distribution with $M_s = 6$ is adopted. For the model with MW-WG dust (Figure 12), curvatures of the attenuation curves at short wavelengths of $\lambda < 0.2\ \mu$m significantly depart not

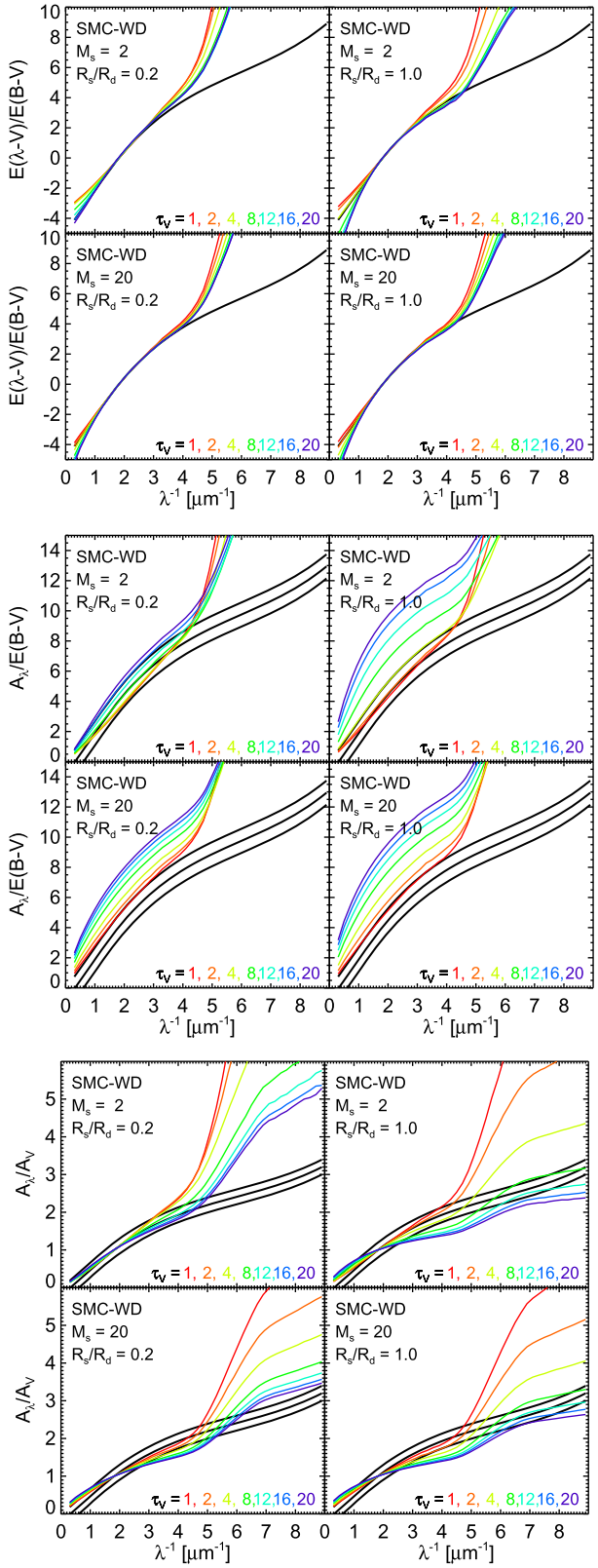

Figure 10. Attenuation curves for the SMC dust of Weingartner & Draine (2001) are plotted in three forms: (top) $E(\lambda-V)/E(B-V)$, (middle) $A_\lambda/E(B-V)$, (bottom) and A_λ/A_V. The black curves denote the Calzetti curve and its uncertainty boundaries.

only from those obtained with the MW-WD dust, as shown in Figure 8, but also from that of the Calzetti curve. On the other hand, the overall shape of the $E(\lambda-V)/E(B-V)$ and

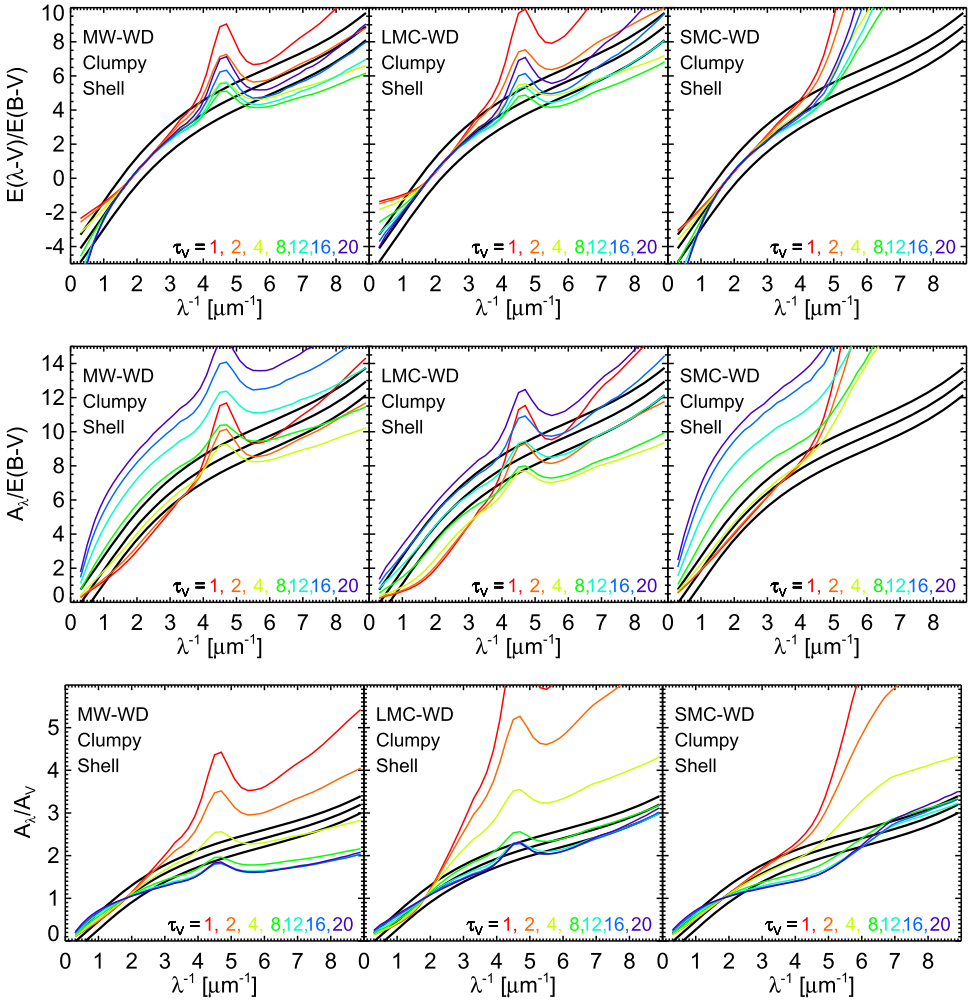

Figure 11. Attenuation curves for (left) the MW, (middle) LMC, and (right) SMC dust types of Weingartner & Draine (2001) in the clumpy media with the shell geometry of Witt & Gordon (2000). The three black curves are the Calzetti curve and its upper and lower boundaries.

A_λ/A_V curves for the SMC-WG dust type (Figure 13), especially with $R_s/R_d \sim 1.0$, are consistent with the Calzetti curve, although the $A_\lambda/E(B-V)$ curves are slightly high. These results are in good agreement with the conclusion of Witt & Gordon (2000). We also confirmed that the attenuation curves of Witt & Gordon (2000)[4] are well reproduced when the MW-WG or SMC-WG dust and the clump shell geometry are assumed. Therefore, the discrepancy between our results and those of Witt & Gordon (2000) is mainly attributed to the difference in the adopted albedo curves. In fact, Inoue et al. (2006) found that the wavelength dependence of the scattering albedo of the underlying extinction curve plays a crucial role in shaping attenuation curves. We also note that Inoue (2005) adopted the MW-WG and SMC-WG dust to model the attenuation curve of an edge-on galaxy using the mega-grain approximation and a plane-parallel geometry, and they found that the attenuation curves calculated with the SMC-WG dust are consistent with the Calzetti curve (see the right panel of Figure 13 in Inoue 2005).

We now show that the shape of the attenuation curve in radiative transfer models is in fact primarily determined by the underlying absorption curve rather than by the extinction curve. It is worthwhile to imagine the case of perfect forward scattering, in which the scattering asymmetry parameter is $g \equiv \langle \cos\theta \rangle = 1$. In this extreme case, the scattered light will always propagate along the initial path, equivalent to the case of no scattering. Then, the emergent light is simply proportional to $\exp(-\tau_{\rm abs})$, where $\tau_{\rm abs}$ is the "absorption" optical depth along the photon direction. In other words, the resulting attenuation curve is completely determined by the absorption curve rather than by the extinction (≡ absorption+scattering) curve. At optical and UV wavelengths, the scattering is quite forward-directed (e.g., Witt et al. 1992a; Draine 2003; Gordon 2004). Therefore, the attenuation curve should be mainly determined by the shape of the adopted absorption curve. In the left panel of Figure 14, the absorption curves for the MW-WD dust and the SMC-WG dust are compared. It is clear that the two absorption curves are very similar, except for the presence of the UV bump feature in the MW-WD dust, while their extinction curves are significantly different (see Figure 3). Therefore, if absorption is the dominant factor, both the MW-WD dust without a UV bump and the SMC-WG dust should equally well reproduce the Calzetti curve.

To further demonstrate our conclusion that the attenuation curve is primarily determined by the shape of the underlying absorption curve, we compare two hypothetical dust types based on the MW-WD dust, as shown in the right panel of Figure 14. In the first dust type, the Drude profile for the

[4] http://dirty.as.arizona.edu/dirty_data/SGE/clumpyII/clumpyII.html

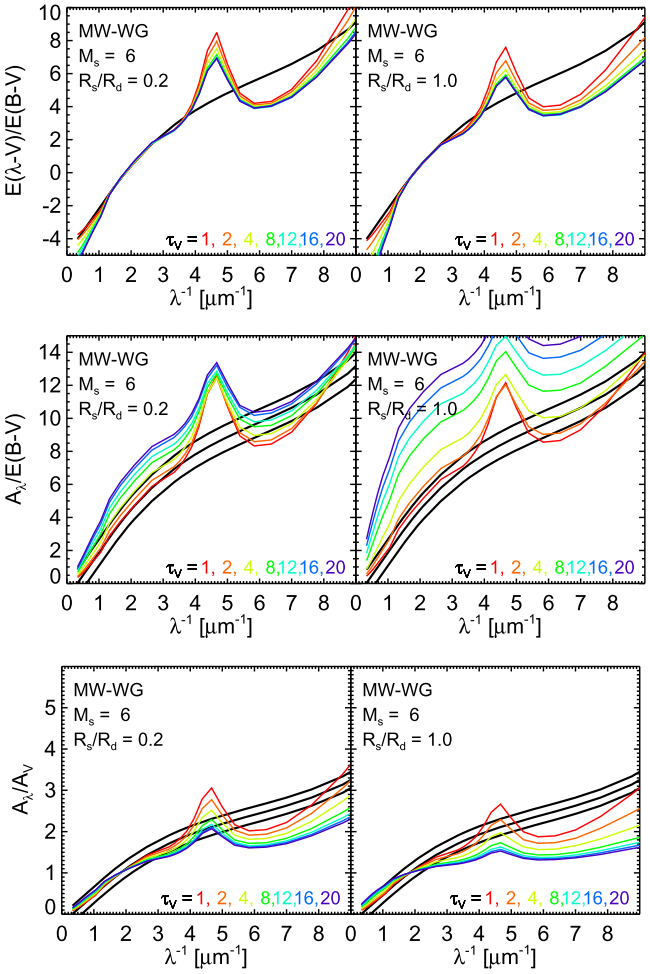

Figure 12. Attenuation curves for the MW dust of Witt & Gordon (2000) in clumpy media with $M_s = 6$ are plotted in three forms: (top) $E(\lambda - V)/E(B - V)$, (middle) $A_\lambda/E(B - V)$, and (bottom) A_λ/A_V. The black curves denote the Calzetti curve and its uncertainty boundaries.

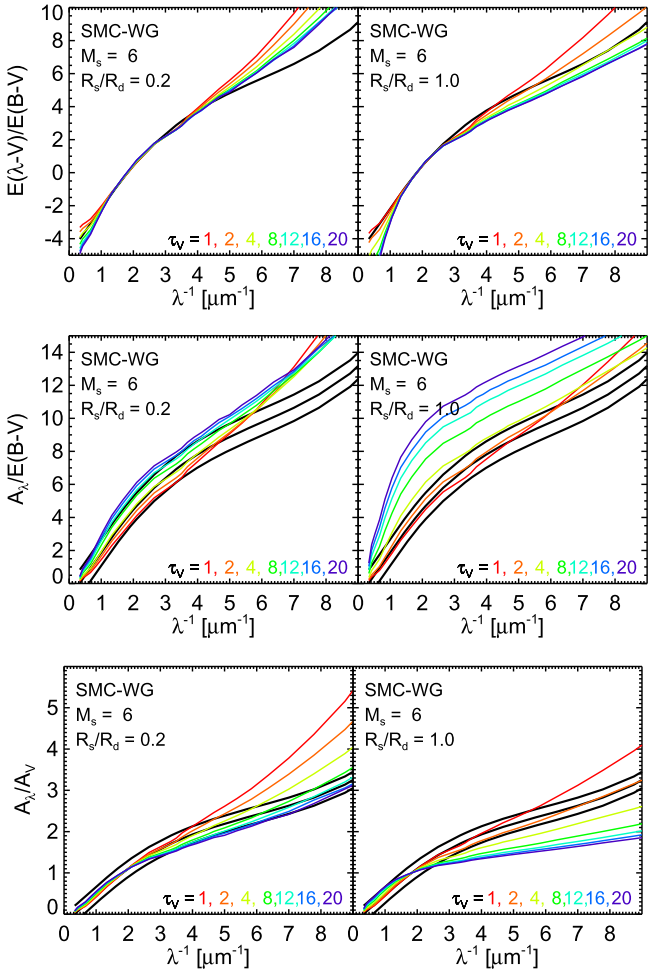

Figure 13. Attenuation curves for the SMC dust of Witt & Gordon (2000) in clumpy media with $M_s = 6$ are plotted in three forms: (top) $E(\lambda - V)/E(B - V)$, (middle) $A_\lambda/E(B - V)$, and (bottom) A_λ/A_V. The black curves denote the Calzetti curve and its uncertainty boundaries.

2175 Å UV bump ($3.5 \leqslant \lambda^{-1} \leqslant 5.7\,\mu\mathrm{m}^{-1}$) feature, as described in Fitzpatrick & Massa (1986, 2007), was removed from the absorption curve. However, the scattering curve remained the same as that of the MW-WD dust. Therefore, the extinction curve near the UV bump is different from that of the MW dust type (black solid lines in the right panel of Figure 14). In the second dust type, the UV bump was assumed to be due to scattering instead of absorption while keeping the extinction curve the same as the original MW-WD extinction curve (red circles in the figure). In other words, the Drude profile for the UV bump was removed from the absorption curve of the MW-WD dust and the removed profile was added to the scattering curve. The scattering phase function was kept the same as that of the MW-WD dust. The extinction curves of these two dust types have different shapes in the wavelength range of the UV bump feature, but their absorption curves are exactly the same.

Radiative transfer calculations were performed to compare the attenuation curves resulting from these two hypothetical dust types. The top and bottom four panels in Figure 15 show the attenuation curves obtained for the first and second dust types, respectively. In the figure, the attenuation curves outside the UV bump wavelength range are exactly the same as the models with a UV bump strength of 1 shown in Figure 8. The attenuation curves with the same R_s/R_d, M_s, and τ_V, but with a different dust type appear to be practically indistinguishable except for the cases with low M_s and R_s/R_d values ($M_s = 2$ and $R_s/R_d = 0.2$ in the figure). Minor differences found for the cases with low M_s and R_s/R_d parameters are attributable to higher effective extinction in the models with a scattering bump, with scattering increasing the probability that the photon will be subsequently absorbed. This example clearly demonstrates that the attenuation curve is mainly determined not by the extinction curve, but by the absorption curve. Differences in the assumed scattering curves yield relatively minor changes in the attenuation curves.

Here, it should be emphasized that the second dust type, in which the UV bump feature is assumed to be caused by scattering, should not be regarded as a physical dust model, but a hypothetical model arbitrarily devised to illustrate the importance of the underlying absorption curve. There is observational evidence that the 2175 Å bump is a pure absorption feature in reflection nebulae NGC 7023 (Witt et al. 1992a) and IC 435 (Calzetti et al. 1995), and the diffuse Galactic light (Witt & Lillie 1973; Lillie & Witt 1976; Morgan et al. 1976)

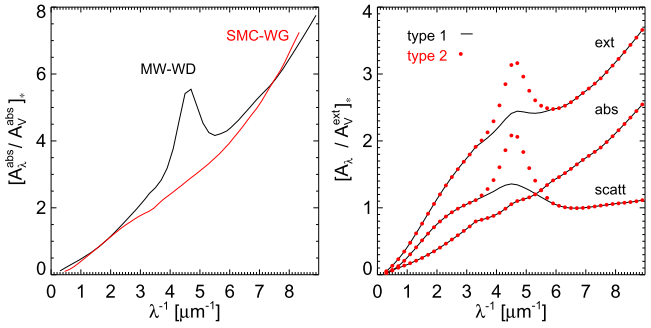

Figure 14. Left panel: comparison of the absorption curves of the MW-WD dust (Weingartner & Draine 2001) and the SMC-WG dust (Witt & Gordon 2000). Right panel: comparison of two hypothetical dust types. The UV absorption bump is removed from the extinction curve in type 1 (black lines). In type 2 (red circles), the bump feature is attributed to scattering. The scattering phase function for the added scattering was assumed to be the same as that of the MW-WD dust.

We showed that variation of the scattering curve produces only minor changes in attenuation curves, provided that the same absorption curve is used and scattering is strongly (but realistically) forward-directed. As g is decreased, multiple scattering becomes more important and the probability for scattered photons to be absorbed somewhere in the medium increases, resulting in higher attenuation. However, if g is a constant over the wavelength range (for instance, $g(\lambda) = 0$), the effect is to increase A_λ by amounts that are almost independent of wavelength; this resulted in no substantial change in the normalized A_λ/A_V curves unless the optical depth is too high. We obtained only slightly shallower attenuation curves (A_λ/A_V) than the original ones when isotropic scattering was assumed over all wavelengths. However, such isotropic scattering could lead to significantly shallower attenuation curves at higher optical depths than those we considered in this paper.

3.4. Variation in Strengths of the UV Bump and PAH Features

The polycyclic aromatic hydrocarbon (PAHs) and/or very small carbonaceous dust grains, which are most likely responsible for the UV absorption bump feature, are susceptible to destruction in hot gas or strong UV radiation field (Omont 1986; Jones et al. 1994; Allain et al. 1996; Micelotta et al. 2010). There is evidence of PAH destruction in the M17 H II region (Povich et al. 2007). Since the Calzetti curve for local starburst galaxies lacks a UV bump feature, it is of interest to vary the UV bump strength and examine resulting variations in the attenuation curves. As discussed in Section 3.3, attenuation curves were calculated by varying the UV bump absorption strength from 0.0 to 0.9 in steps of 0.1 relative to that of the MW-WD extinction curve. In the left panels of Figure 16, the absorption curves with a UV bump strength varying from 0.0 to 0.8 in steps of 0.2 relative to that of the MW-WD dust are shown in grayscale. Some representative results are shown in Figure 17 for the MW-WD dust type with a UV bump strength of 0.1 and 0.4. A dust extinction curve with no UV absorption bump was shown in Section 3.3 (see the bottom panels of Figure 15). Although a detailed analysis of the detectability of a weak UV bump is beyond the scope of the present study, a UV bump feature with a strength of $\lesssim$0.1 appears to be undetectable at present, especially in the low

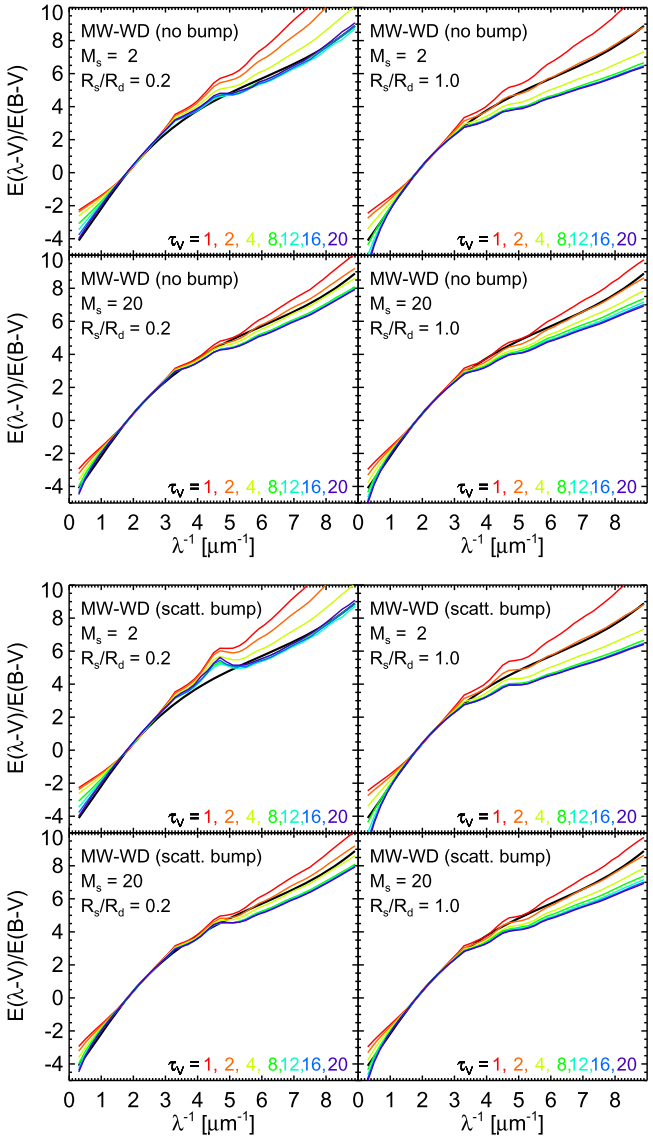

Figure 15. Attenuation curves for two hypothetical dust types. In the top four panels, the UV bump was removed from the MW-WD extinction curve (type 1). In the bottom four panels, the UV absorption bump feature was replaced by a scattering feature with the same strength (type 2). The Calzetti curve is also shown in black.

signal-to-noise ratio (S/N) *IUE* spectra used to derive the Calzetti curve and in broad- or narrowband photometric SED data. Even with a stronger UV bump strength, for instance 0.4, the bump feature in the attenuation curves with $M_s \sim 20$, $R_s/R_d \sim 1$, and $\tau_V \gtrsim 4$ would be hardly noticeable in low-S/N spectra or photometric data.

Here, it should be noted that not only the UV absorption bump, but also some part of "the FUV extinction rise" in the MW extinction curve may be produced by PAHs or small carbonaceous dust grains (e.g., Li & Draine 2001; Mishra & Li 2015). If PAHs or small carbonaceous dust grains are responsible for both the UV bump and the FUV extinction rise, it may be unphysical to arbitrarily reduce only the UV bump strength while keeping the FUV rise the same. Therefore, the strength of the whole model PAH contribution to the optical-UV absorption—including the UV bump and absorption at $\lambda < 2000$Å—was also varied from 0.0 to 0.9 relative to that of the MW-WD dust to examine its effect on the attenuation

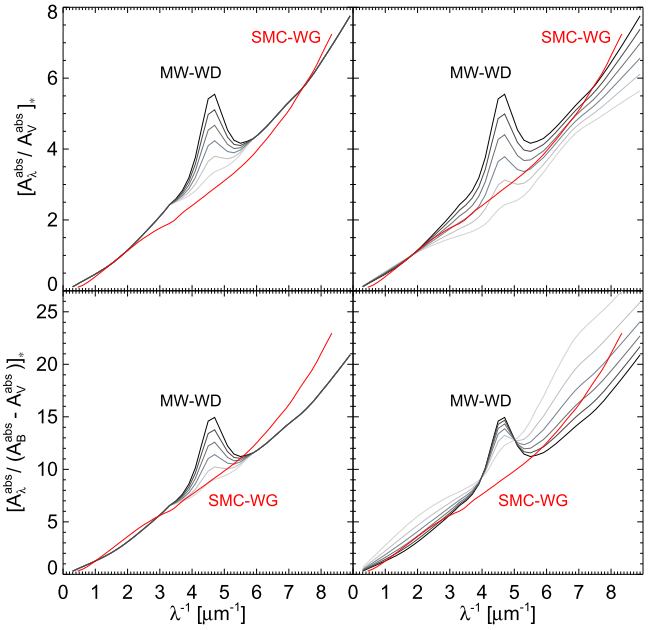

Figure 16. Absorption curves with lower (left) UV bump and (right) PAH features are shown in grayscale. The strengths of the features were reduced from 0.8 to 0.0 in steps of 0.2 relative to those of the MW-WD dust. The absorption curves are normalized by (top) $[A_V^{abs}]_*$ and (bottom) $[A_B^{abs} - A_V^{abs}]_*$. The absorption curve of the SMC-WG dust is also shown in red.

curve. The right panels in Figure 16 show variations of the absorption curve as the strength of the PAH feature, including both the UV bump and FUV extinction rise features, decreases from 0.8 to 0.0. We decreased the strengths of the UV bump and PAH features by scaling down the absorption cross section of PAHs given in Li & Draine (2001). Figures 18 and 19 show the attenuation curves calculated assuming the PAH contribution to be 0.0 and 0.4, respectively, relative to the standard MW-WD model. Unlike the cases (Figure 17) in which only the UV bump strength is reduced, the overall shape of the attenuation curves as well as the bump strength is changed. In general, the $E(\lambda - V)/E(B - V)$ curves become slightly steeper at UV wavelengths and the R_V values in the $A_\lambda/E(B - V)$ curves become higher. This is because the PAHs absorb not only UV photons, but also optical photons (Li & Draine 2002). The absorption cross section of PAHs at B band is higher than that at V band, and thus the reduction of the PAHs feature results in less absorption at B band than at V band. Consequently, $E(B - V)$ is decreased and R_V is increased. This leads the $E(\lambda - V)/E(B - V)$ curves to become steeper in the UV, and the $A_\lambda/E(B - V)$ curves to fail to reproduce the Calzetti curve. On the other hand, the A_λ/A_V curves become shallower in general. The A_λ/A_V curves without PAHs in Figure 18 are consistent with the Calzetti curve outside the UV bump wavelength range, but show a wide dip-like feature near the UV bump. This apparent dip is mainly due to a steep increase in the absorption (a drop in the albedo) of the silicate grains with decreasing wavelength near 2000 Å. The A_λ/A_V curves with the PAH feature strength of 0.4 in Figure 19 are very similar to the Calzetti curve, except for the presence of a weak UV bump. The attenuation curves have slightly higher R_V values than the Calzetti curve. We note that the shapes of the $E(\lambda - V)/E(B - V)$ and $A_\lambda/E(B - V)$ curves in Figures 18 and 19 are direct consequences of the $[A_\lambda^{abs}/(A_B^{abs} - A_V^{abs})]_*$ curves shown in the bottom right panel of Figure 16. The $[A_\lambda^{abs}/(A_B^{abs} - A_V^{abs})]_*$ curves with weaker strength of PAHs have steeper slopes in the UV and higher values of $[A_V^{abs}/(A_B^{abs} - A_V^{abs})]_*$. It can also be found that the properties of the A_λ/A_V curves are mainly caused by the shape of the $[A_\lambda^{abs}/A_V^{abs}]_*$ curves shown in the top right panel of Figure 16.

In the above models, the strength of the UV bump feature was assumed to be uniformly reduced over the whole dusty medium. However, the carriers of the features may be preferentially destroyed only in hot gas or near strong UV stars. To examine this possibility, we consider a case where PAHs are completely destroyed in regions with less than a certain critical density but remain unaffected in higher density regions. The critical density ρ_c was selected such that the fraction of cumulative mass defined by

$$f_{\rm destr} \equiv \sum_{\rho_i \leqslant \rho_c} \rho_i / \sum_i \rho_i \quad (5)$$

varies from 0.1 to 0.9 in steps of 0.1, where ρ_i is the density of each cell. Thus a fraction $f_{\rm destr}$ of the PAHs are assumed to have been destroyed. Figure 20 shows the attenuation curves for $f_{\rm destr} = 0.6$ and 0.3. As can be noted in the figure, the UV bump feature is much weaker and the shape is grayer than in the former models, in which the same amount of PAHs was uniformly depleted over the entire volume (e.g., the models with $f_{\rm PAH} = 1 - f_{\rm destr}$). This is because the low-density regions with no PAHs take up most of the volume although the regions contain only a small fraction of total dust mass, as shown in Figure 2; in other words, high-density regions containing PAHs and most of the dust mass occupy only a relatively small volume. Consequently, most photons pass through locations with no PAHs, and the resulting attenuation curves have much weaker PAH features than in the case with uniformly mixed PAHs.

3.5. Starlight Originating from Dense Regions

One more aspect to be considered is that bright early-type stars from which most UV light originates are mainly located near spatially localized dense regions. We therefore examined the attenuation curves of the case in which the stellar source is uniformly distributed, but only in regions where the dust density is above some critical value. The fraction of cumulative mass measured from the highest density cell, as opposed to Equation (5), was varied from 0.1 to 0.9 in steps of 0.1. However, we found no significant differences to the models with a uniform stellar distribution shown in Figure 8; the attenuation curves showed virtually no change in the slope (δ) defined in the next section, and the UV bump strength (E_b) was only slightly lowered, by less than 5%. For test purposes, we also calculated models in which photons only originated from low-density regions. No significant differences were found, however; the slope δ slightly increased, by ~4% (shallower attenuation curve). This is because most of the starlight attenuation occurs while photons pass through dense regions. The probability of passing through high-density regions is not significantly altered by the distribution of stellar locations when we mainly consider attenuation curves that are averaged over all directions.

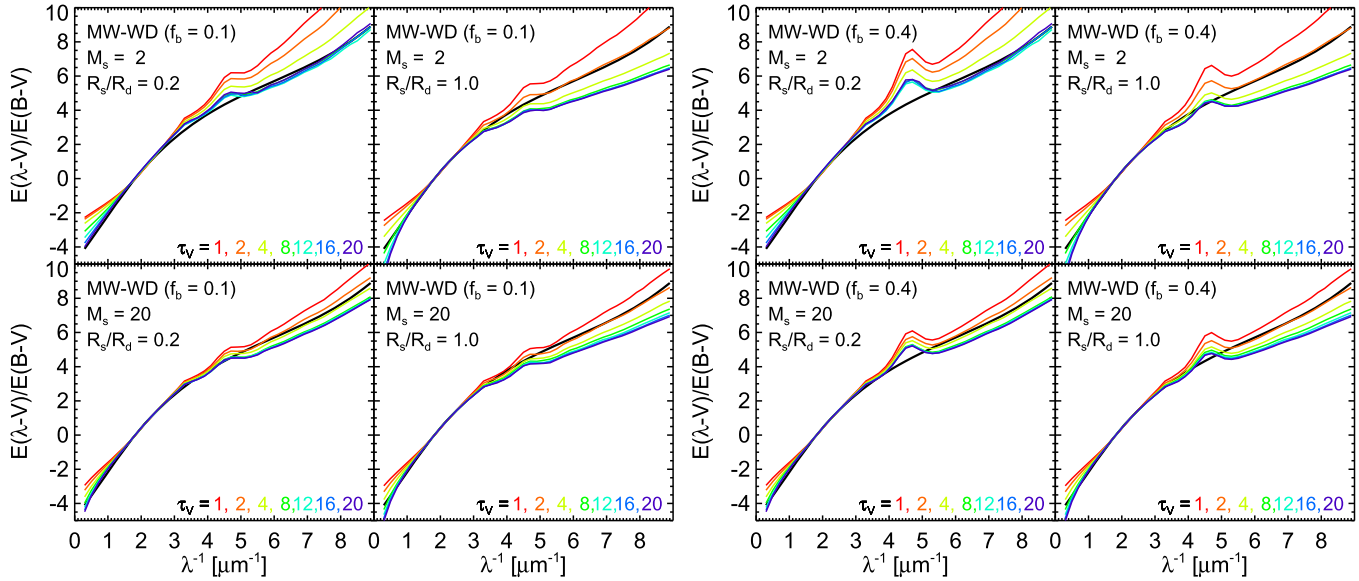

Figure 17. Attenuation curves for two dust types with UV bump strengths of (left) 0.1 and (right) 0.4 relative to that of the MW-WD. The Calzetti curve is also shown in black.

Therefore, the UV absorption bump strength is mainly determined by the abundance of the UV bump carriers. As can be noted in Figure 8 and in the next section (Figure 21), the UV bump can be almost completely suppressed through radiative transfer effects at high optical depths ($\tau_V \gtrsim 20$); the suppression of the bump is prominent in the A_λ/A_V attenuation curves, but is less clear in forms of $A_\lambda/E(B-V)$ and $E(\lambda-V)/E(B-V)$. However, the attenuation curves with a strongly suppressed UV bump are much shallower than the Calzetti curve. The result is consistent with that of Witt & Gordon (2000) in that the Calzetti curve can be reproduced only with an extinction curve with no or a very weak UV bump. This point is discussed further in Section 4.2.

3.6. Correlation Between Slope and UV Bump Strength

The model attenuation curves reveal a large variation in both overall shape and UV bump strength; the slope of the attenuation curve tends to correlate with the UV bump strength. In other words, the UV bump can be suppressed through radiative transfer effects, but at the expense of a gray attenuation (Witt & Gordon 2000). Kriek & Conroy (2013) found a strong correlation between the attenuation curve slope and UV bump strength from a large sample of star-forming galaxies, which is qualitatively consistent with radiative transfer calculations. To quantitatively compare with our radiative transfer model results, we adopted the modified Calzetti function proposed by Noll et al. (2009a), which is represented by

$$A_\lambda = \frac{A_V}{k(V)}[k(\lambda)+D(\lambda)]\left(\frac{\lambda}{\lambda_V}\right)^\delta, \quad (6)$$

where $k(\lambda)$ indicates the Calzetti curve and δ is employed to allow variation in the slope of the attenuation curve: $\delta > 0$ corresponds to shallower attenuation. The Calzetti curve (Calzetti et al. 2000) is given by

$$\begin{aligned} k(\lambda) &= 2.659(-1.857 + 1.040/\lambda) \\ &\quad + R_V,\ 0.63\mu\mathrm{m} \leqslant \lambda \leqslant 2.20\mu\mathrm{m}; \\ &= 2.659(-2.156 + 1.509/\lambda - 0.198/\lambda^2 \\ &\quad + 0.011/\lambda^3) + R_V,\ 0.12\mu\mathrm{m} \leqslant \lambda \leqslant 0.63\mu\mathrm{m}, \end{aligned} \quad (7)$$

where $R_V = 4.05 \pm 0.80$. The UV bump feature is represented by the Drude profile, which is defined by

$$D(\lambda) = \frac{E_b(\lambda\Delta\lambda)^2}{(\lambda^2-\lambda_0^2)^2+(\lambda\Delta\lambda)^2}, \quad (8)$$

where λ_0, $\Delta\lambda$, and E_b are the central wavelength, width, and strength (peak height) of the profile. The central wavelength of the UV bump is assumed to be $\lambda_0 = 0.2175\ \mu$m and the width of the bump is $\Delta\lambda = 0.035\ \mu$m, which were found by Noll et al. (2009a) from a stack of spectra of high-redshift galaxies. Using this profile, Kriek & Conroy (2013) derived a linear relation between δ and E_b given by

$$E_b = (0.85 \pm 0.09) - (1.9 \pm 0.4)\delta. \quad (9)$$

We fitted our attenuation curves with the modified Calzetti function (Equation (6)). Figure 21 shows the best-fits for (top) the MW-WD and (bottom) LMC-WD dust-type models. The left panels show the attenuation curves (dot symbols) together with the best-fit curves (connected lines). It is clear that the modified Calzetti curve (Equation (6)) fairly well reproduces the attenuation curves calculated with both dust types.

The right panels in Figure 21 show the correlations between the two best-fit parameters (E_b and δ), in which the black and blue lines represent the best linear-fit functions of E_b versus δ from our results and the linear relationship of Kriek & Conroy (2013), respectively. The best-fit line shown in the last panel of each dust type was obtained by equally weighting all the (E_b, δ) pairs estimated from attenuation curves. The basic properties discussed in the previous sections are confirmed in the figure. The shallowness of the attenuation curve anticorrelates with the UV bump strength. The attenuation curves are shallower (more

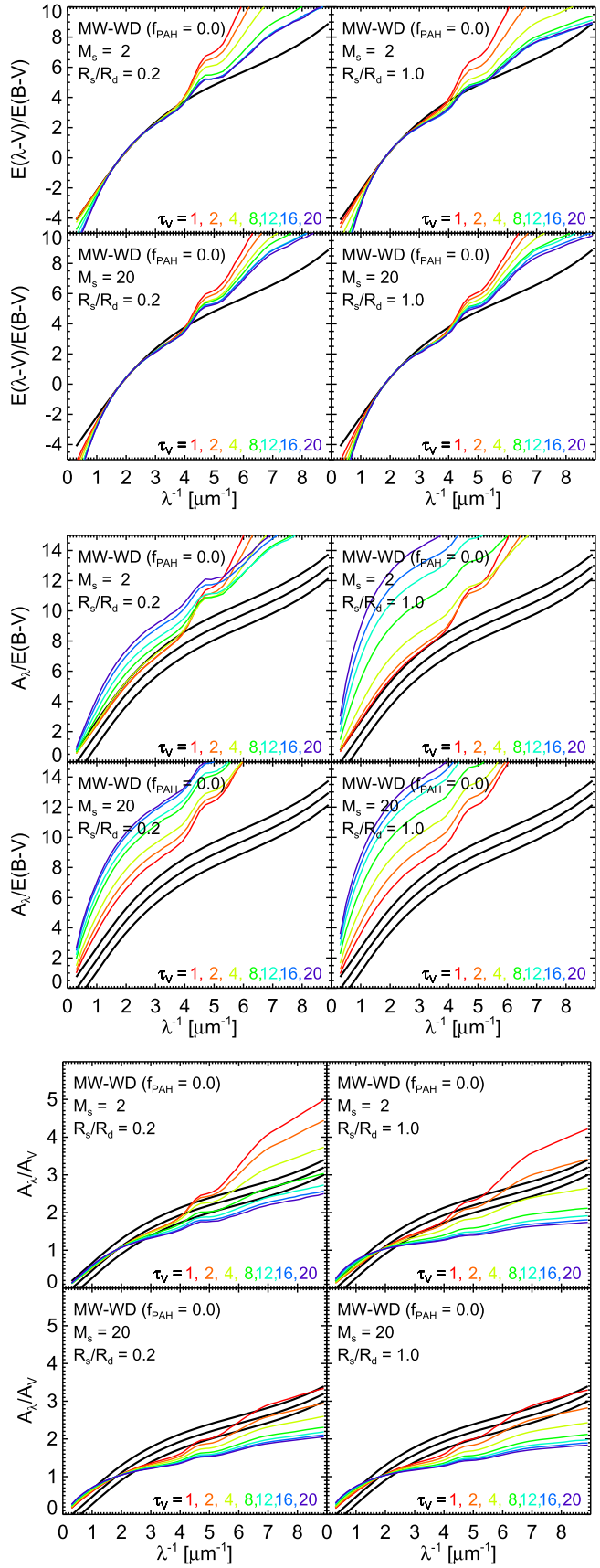

Figure 18. Attenuation curves for a dust type with no PAH absorption (UV bump + FUV extinction rise). The curves are shown in three forms: (top) $E(\lambda - V)/E(B - V)$, (middle) $A_\lambda/E(B - V)$, and (bottom) A_λ/A_V. The Calzetti curve and its uncertainty range are also shown in black.

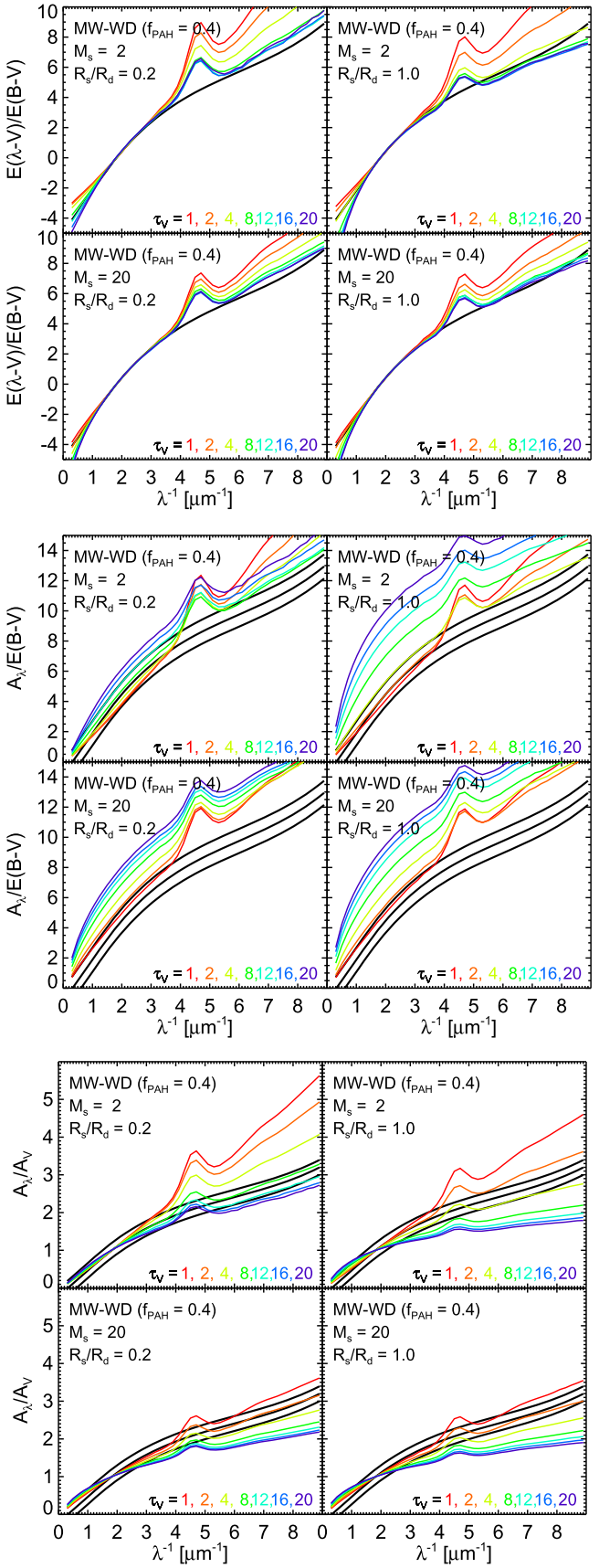

Figure 19. Attenuation curves for a dust type for which the abundance of PAHs is 0.4 of the MW-WD dust. The curves are shown in three forms: (top) $E(\lambda - V)/E(B - V)$, (middle) $A_\lambda/E(B - V)$, and (bottom) A_λ/A_V. The Calzetti curve and its uncertainty range are also shown in black.

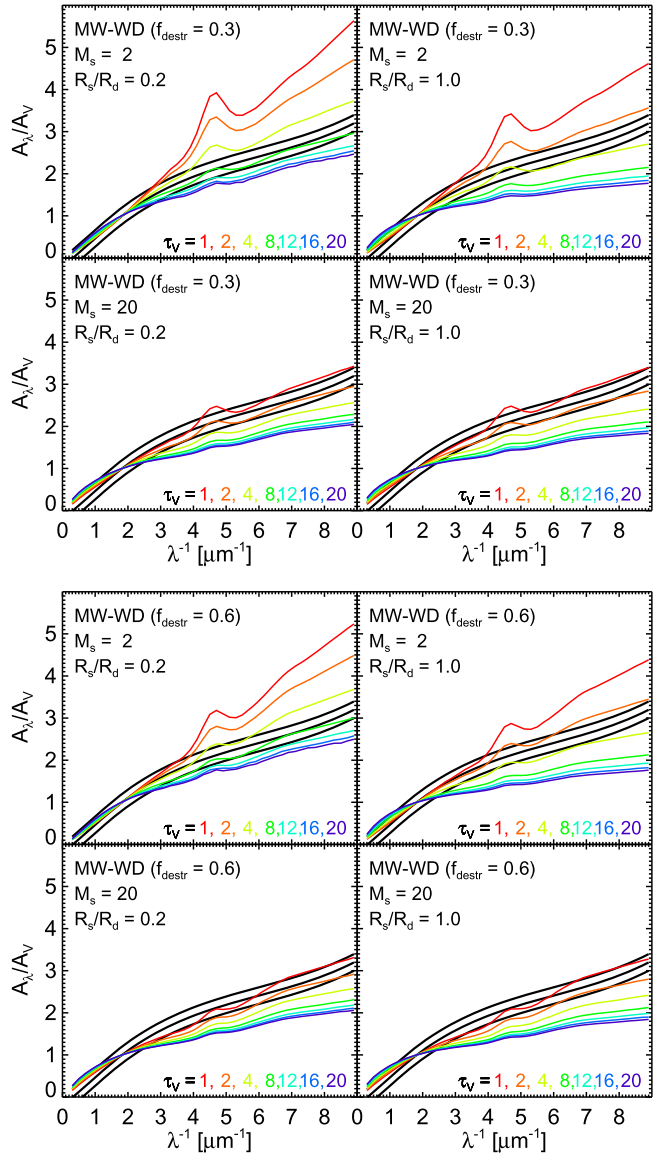

Figure 20. Attenuation curves (A_λ/A_V) for the case in which PAHs are destroyed in low-density regions having (top) 30% and (bottom) 60% of dust mass. The Calzetti curve and its uncertainty range are also shown in black.

positive δ) and have weaker UV bumps (smaller E_b) for higher R_s/R_d, τ_V and M. The attenuation curves derived from the LMC-WD dust are slightly steeper than those from the MW-WD dust and have a slightly stronger UV bump strength for a given set of parameters (R_s/R_d, τ_V and M). This is simply because the extinction curve $[A_\lambda/A_V]_*^{\rm LMC}$, relative to $[A_V]_*^{\rm LMC}$, of the LMC dust is steeper and has a stronger UV bump feature than for the MW curve $[A_\lambda/A_V]_*^{\rm MW}$, as shown in the bottom left panel of Figure 3. However, note that the LMC extinction curve $[A_\lambda/N_{\rm H}]_*^{\rm LMC}$ per hydrogen column density has a weaker UV bump than the MW curve $[A_\lambda/N_{\rm H}]_*^{\rm MW}$. The slopes for the LMC-WD dust range from $\sim$–1.5 to $\sim$0.2, which are on average smaller (steeper) than those of Kriek & Conroy (2013), which range from $\sim$–0.5 to $\sim$0.3. On the other hand, the MW-WD dust produces slopes that are consistent with the observational result of Kriek & Conroy (2013). The UV bump strength in both dust types is, however, much higher than the observational result. We also note that the UV bump strength (E_b) for the LMC-WD dust is higher than for the MW-WD for a given slope (δ); in other words, E_b for the LMC-WD dust increases faster than that of the MW-WD dust as δ decreases.

The linear relationships between E_b and δ in Figure 21 are steeper than the result of Kriek & Conroy (2013), indicating that a weaker UV bump strength is required to explain their result. Figure 22 shows the best-fit results for the models with (top) a UV bump strength of 0.3 and (bottom) a PAH feature strength of 0.4, which both appear to well reproduce the relation of Kriek & Conroy (2013). Note that the equivalent optical depth of $\tau_V = 20$ mostly corresponds to A_V values lower than 3, except for the cases with the lowest R_s/R_d and M_s values, as seen in Figure 5. This upper limit of A_V in our results is consistent with the range of the best-fit A_V estimated in Kriek & Conroy (2013). We also note that there is a correlation between δ and A_V in their Figure 2(a) if a single red data point at (δ, E_b) $\sim$ (-0.44, 2.3) is ignored, implying a correlation of the slope of the attenuation curve with the effective optical depth τ_V. This trend is consistent with that shown in the last (lower right) panels for each dust type in Figure 22, in which every dot corresponds to a single radiative transfer model and the colors of the dots reflect the A_V of the individual models. The overall correlation between A_V and δ is clearly shown in the figure. Therefore, our results strongly suggest that the anticorrelation between E_b and δ found in Kriek & Conroy (2013) may be due to radiative transfer effects. The abundance of the UV bump carriers or PAHs in the sample of Kriek & Conroy (2013) would be 30% or 40% of that of the MW-WD dust, if the carriers are assumed to be uniformly mixed throughout the dusty ISM.

We also fitted the attenuation curves obtained for the cases in which the PAHs are destroyed only in low-density regions. Figure 23 shows the results for two cases in which the PAHs are destroyed in low-density regions of which the accumulated mass fraction ($f_{\rm destr}$) is 0.3 and 0.5. In this model type, the relation between E_b and δ could not be uniquely quantified because of a bimodality, as shown in Figure 23. The best-fit E_b values for most of the models with $f_{\rm destr} \gtrsim 0.5$ were found to be approximately zero, indicating no bumps, while most of the models with $f_{\rm destr} \lesssim 0.2$ gave steeper linear relationships between E_b and δ than that of Kriek & Conroy (2013). For the intermediate cases of $f_{\rm destr} = 0.3$ and 0.4, the attenuation curves with high M_s and τ_V gave best-fit values of $E_b \approx 0$. On the other hand, relationships between E_b and δ steeper than that of Kriek & Conroy (2013) were found for low M_s and τ_V, as shown for $M_s = 2$ in Figure 23. The models that gave $\delta \sim 0$ seem to indicate that galaxies having PAHs strongly depleted in low-density regions would lack the UV bump feature in their attenuation curves. However, these models with $\delta \sim 0$ showed wavy structures in the attenuation curves that slightly deviated from the modified Calzetti curve. We also note that most of the volume has no PAHs in these models even for $f_{\rm destr} = 0.3$, as shown in Figure 2. This model for the PAH abundance does not appear to be consistent with observations.

3.7. Correlation Between Slope and Color Excess

Salmon et al. (2016) applied a Bayesian analysis to a photometric sample of galaxies at $z \sim 2$ and found an average relation between the attenuation curve slope (δ) and the $E(B-V)$ color excess given by

$$\delta = (0.62 \pm 0.05)\log[E(B-V)] + 0.26 \pm 0.02. \quad (10)$$

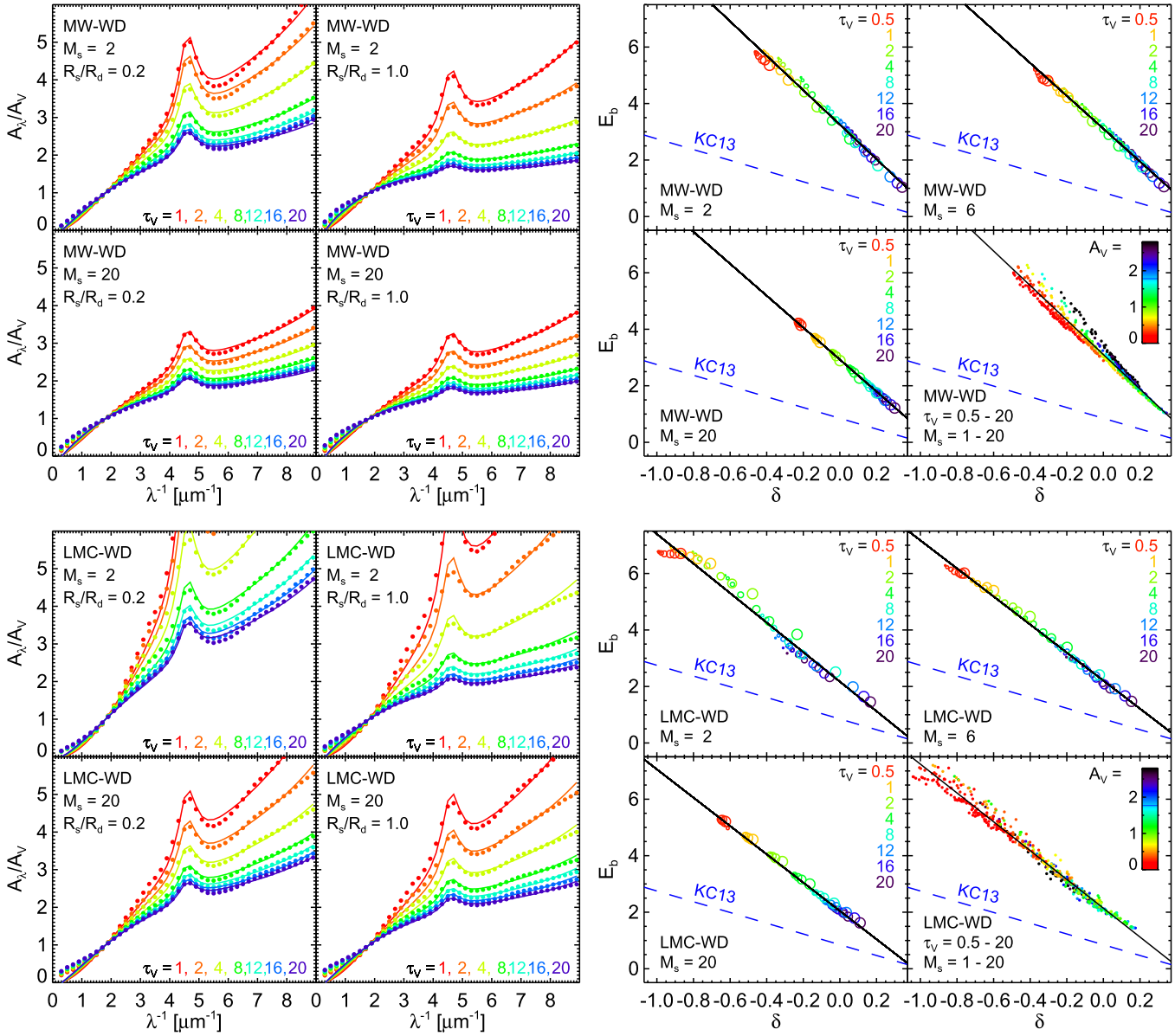

Figure 21. Best-fit results to the modified Calzetti curve. The top and bottom panels show the fitting results for the attenuation curves calculated with the MW-WD dust and the LMC-WD dust, respectively. In the left panels, the attenuation curves for each dust type are shown as filled circles, and the best-fitting modified Calzetti curves are overplotted as lines with the same colors as the circles. In the right panels, the best-fit bump strength (E_b) and slope (δ) are compared for the models with three Mach numbers ($M_s = 2$, 6, and 20). The black lines in the right panels are the best-fit linear functions for the E_b vs. δ relationships; the linear relationship given in Kriek & Conroy (2013) is shown as blue dashed lines. The color of the circles denotes the homogeneous optical depth (τ_V), except in the last panels, for each dust type. The size of the open circles in the right panels reflects the size of the stellar distribution ($R_s/R_d = 0.0$, 0.2, 0.4, 0.6, 0.8, 0.9, and 1.0). The last panel in each dust type shows the relationship between the best-fit parameters (E_b and δ) estimated from all attenuation curves, and the color of the dots now indicates A_V values for individual attenuation curves. The best-fit lines shown in the last panels, which were obtained by equally weighting the (E_b, δ) values for all attenuation curves, are $E_b = (3.11 \pm 0.01) - (6.10 \pm 0.04)\delta$ for the MW-WD dust models and $E_b = (2.14 \pm 0.01) - (5.10 \pm 0.03)\delta$ for the LMC-WD dust models.

The equation was derived by binning the joint posterior distribution $P(E(B-V), \delta)$ of $E(B-V)$ and δ and then fitting the median δ for each bin of $E(B-V)$ as a function of $E(B-V)$. They also showed that radiative transfer models of Witt & Gordon (2000) are consistent with this equation.

In Sections 3.1 and 3.2, we noted that attenuation curves become grayer as the homogeneous optical depth τ_V increases. Therefore, the observed correlation between δ and $E(B-V)$ may be a natural consequence of radiative transfer effects. To compare Equation (10) with our results, Figure 24 shows the δ versus $E(B-V)$ relations for (top) the MW-WD, (middle) LMC-WD, and (bottom) SMC-WD dust types. In the figure, clumpiness increases from the left ($M_s = 1$) to the right ($M_s = 20$) panels. The variation in the UV absorption bump strength did not significantly alter the best-fit slope δ; therefore, the δ versus $E(B-V)$ relations with a varying UV bump strength in the MW-WD models were virtually the same as shown in Figure 24. In Figure 24, Equation (10) is best matched by the MW-WD models with $M_s \sim 2$ and $R_s/R_d \sim 0.8$, LMC-WD models with $M_s \sim 20$ and $R_s/R_d \sim 0.8$, and/or SMC-WD models with $M_s \sim 6$ and $R_s/R_d \sim 0.6$. In our models, the correlation between δ and $E(B-V)$ is attributed to their dependence on the optical depth τ_V; attenuation curves become shallower (larger δ) and

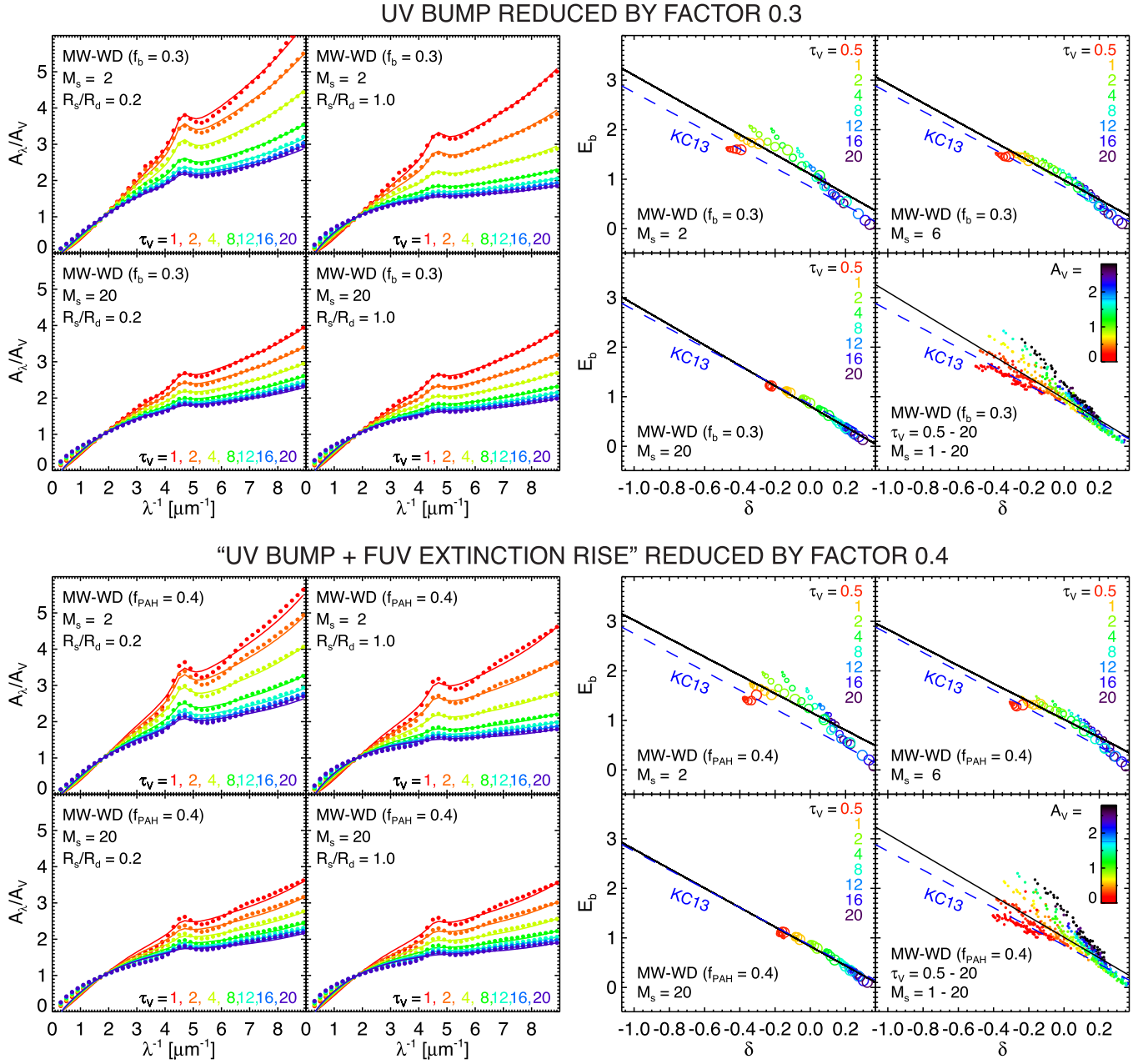

Figure 22. Best-fit results to the modified Calzetti curves. The top panels show the results for the dust type with a UV bump strength of 0.3 ($f_b = 0.3$) relative to that of the MW-WD dust. The bottom panels show the results for the dust type in which the contribution of the PAH component is reduced by a factor 0.4 ($f_{\rm PAH} = 0.4$). In the last panels of each dust type, the best linear fits between the bump strength and slope are $E_b = (0.96 \pm 0.01) - (2.15 \pm 0.04)\delta$ for the model with $f_b = 0.3$ and $E_b = (1.01 \pm 0.01) - (2.08 \pm 0.05)\delta$ for the model with $f_{\rm PAH} = 0.4$. The blue dashed line labeled KC13 is the empirical linear relationship found by Kriek & Conroy (2013). See also the caption of Figure 21 for further explanation.

output SEDs become redder as the optical depth increases. The left panels of Figures 7 and 18 in Salmon et al. (2016) show that relatively massive galaxies in the spectroscopic redshift sample have shallow attenuation curves (denoted by "starburst-dust" in the figures), while less massive galaxies have steeper attenuation curves ("SMC92-dust") if a data point with stellar mass of $\sim 10^{11.5}\,M_\odot$ is ignored. This is consistent with our results that the slope δ increases with increase of τ_V. However, the trend appears to disappear in the more complete, photometric redshift sample (B. Salmon 2016, private communication).

Figure 24 also shows large variations in the relation between δ and $E(B-V)$ as a result of variation in Mach number ($M_{\rm s}$) and/or the stellar distribution size ($R_{\rm s}/R_{\rm d}$). In general, δ becomes larger (shallower) and $E(B-V)$ becomes smaller as $M_{\rm s}$ and/or $R_{\rm s}/R_{\rm d}$ increase. The properties were also noted in Sections 3.1 and 3.2. Therefore, large variations in the δ versus $E(B-V)$ diagram shown in Figures 9 and 11 of Salmon et al. (2016) may be attributable to the diversity of $M_{\rm s}$ and $R_{\rm s}/R_{\rm d}$ rather than to variation in the intrinsic dust properties.

Figure 25 shows the relation of δ versus A_V, which is also convenient for interpreting observational results. In the figure, we also compare with the relation derived from Equation (10) for $R_V = A_V/E(B-V) = 4.05 \pm 0.80$ as in the Calzetti curve. The relation of δ versus A_V leads to conclusions similar to those described for Figure 24, except that the LMC-WD dust

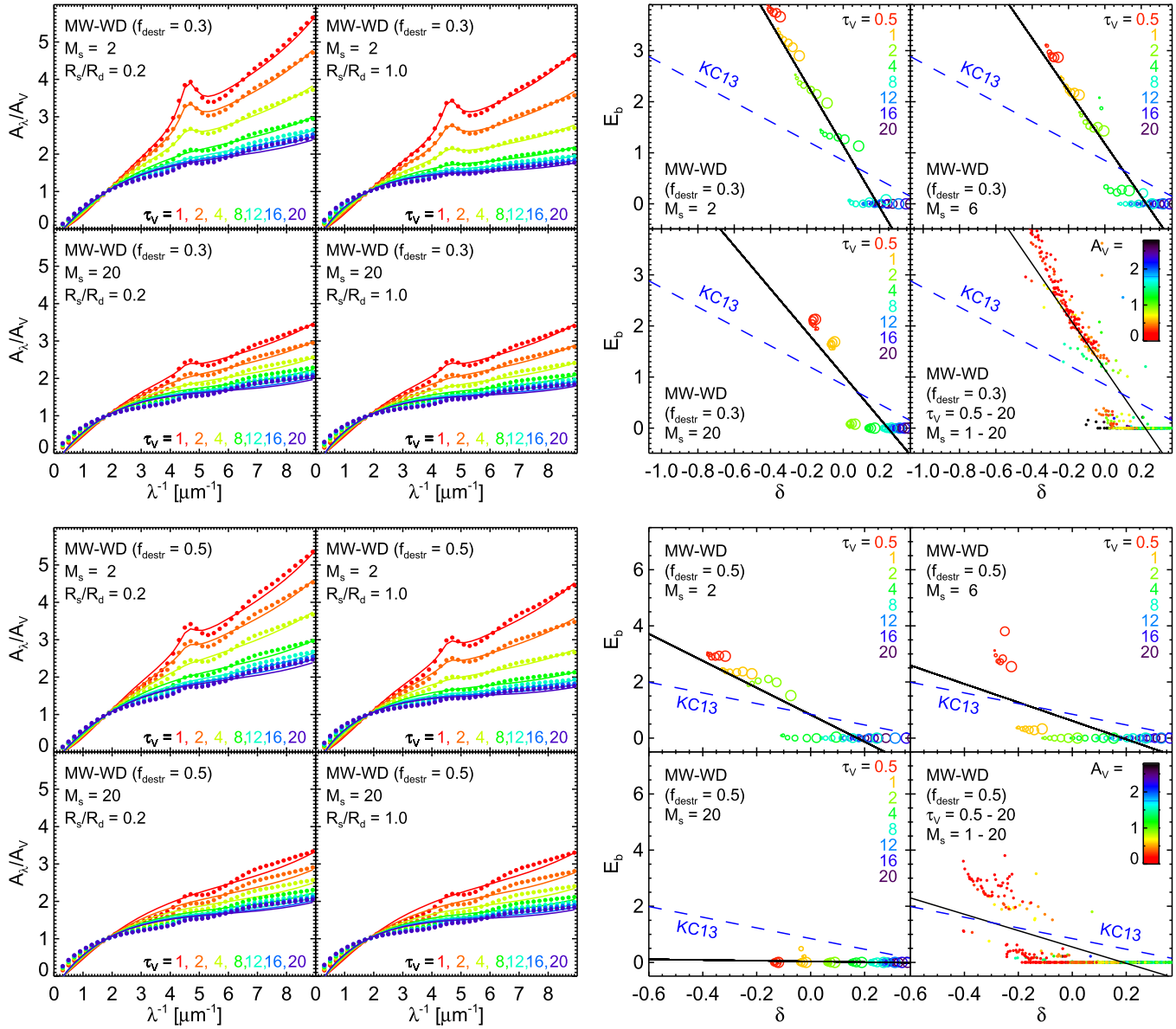

Figure 23. Best-fit results to the modified Calzetti curves for the case in which PAHs are destroyed in low-density regions whose fractional dust mass is (top) 30% and (bottom) 50%. The best linear fits between the bump strength and slope are (top) $E_b = (0.98 \pm 0.03)-(4.57 \pm 0.14)$ for $f_{\rm destr} = 0.3$ and (bottom) $E_b = (0.39 \pm 0.04)-(2.00 \pm 0.19)$ for $f_{\rm destr} = 0.5$. See also the caption of Figure 21 for further explanations.

type (with $M_{\rm s} \sim 10$ and $R_{\rm s}/R_{\rm d} \sim 0.8$) now best matches the relation inferred from Equation (10). However, we note that intrinsic dust properties are not well constrained with only the observational data of δ versus $E(B-V)$ or δ versus A_V. The MW-WD and SMC-WD dust types can both equally well explain the observational data of Salmon et al. (2016), but the attenuation curves derived with the SMC-WD dust type are not consistent with the overall shape of the Calzetti curve as shown in Figure 10. The MW-WD model with a UV bump strength reduced by a factor of ∼0.3–0.4 is preferred to explain the observational attenuation curves of star-forming galaxies, as described in Sections 3.2 and 3.6.

4. DISCUSSION

We showed that the primary determinant of the attenuation curve is not the underlying extinction curve, but the absorption curve. Inoue et al. (2006) studied the UV color variation by varying the wavelength dependence of the scattering albedo while keeping the MW extinction curve, finding a strong effect of the adopted albedo on the UV color. This result implies that the attenuation curve in galaxies would strongly depend on the underlying albedo curve. This agrees well with our result in that the variation of albedo is in fact equivalent to a variation of absorption. We also note that no scattering effect was considered in the turbulent media foreground screen models of Fischera et al. (2003) and Fischera & Dopita (2005, 2011). Fischera et al. (2003) stated that it is somewhat surprising that their attenuation model works well even without the inclusion of scattered light. In fact, this is not surprising because absorption is the most important factor in producing attenuation curves.

As noted in Buat et al. (2012), radiative transfer models, including ours and those of Witt & Gordon (2000), indicate that SED fitting codes must allow for variations of the attenuation curve to fit the UV continuum of galaxies. Our

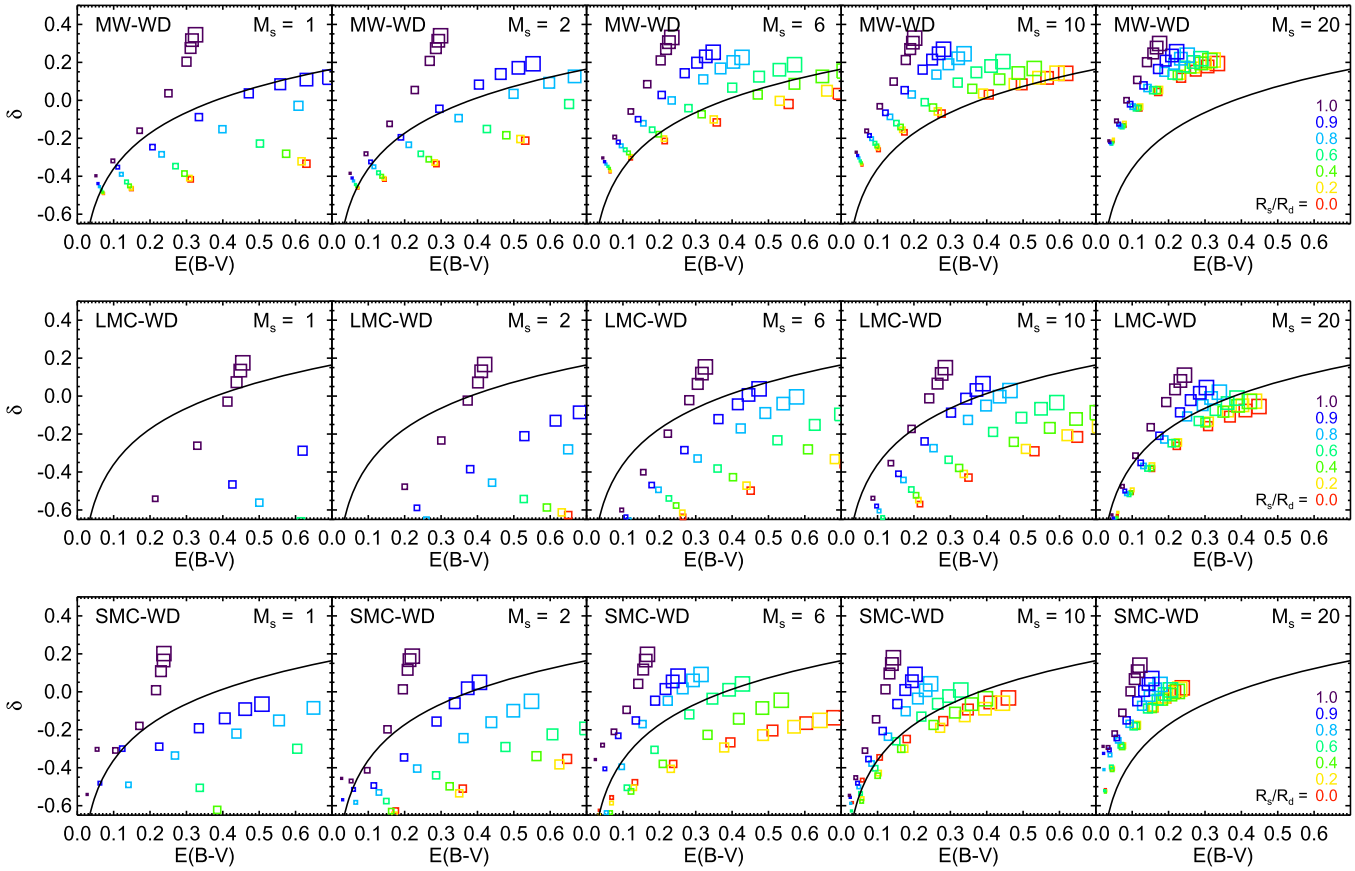

Figure 24. Correlation between the attenuation curve slope δ and $E(B-V)$ for (top) the MW, (middle) LMC, and (right) SMC dust types of Weingartner & Draine (2001). The color of the squares denotes the size of the stellar distribution (R_s/R_d = 0.0, 0.2, 0.4, 0.6, 0.8, 0.9, and 1.0), as shown in the rightmost panels. The size of the squares reflects the homogeneous optical depth τ_V (=0.5, 1, 2, 4, 8, 12, 16, and 20). The smaller square corresponds to lower τ_V. The black curve denotes the relationship for δ and $E(B-V)$ given by Salmon et al. (2016). Note that the color change in this figure shows the variation of R_s/R_d, whereas it represents the variation of τ_V in Figures 21–23.

radiative transfer results for a wide range of configurations considered in the present paper indicate that the modified Calzetti curve (Equation (6)) is versatile enough to reproduce theoretical attenuation curves and to model galactic SEDs.

In the following, we further discuss three topics that are relevant to our results.

4.1. Observational Discrimination between Dust Models

In the present study, we favor the MW dust model of Weingartner & Draine (2001) with the UV bump suppressed. There is no direct observational evidence of a preference for one dust model over another in external star-forming or starburst galaxies. In this regard, we note that there is no empirical study on the values of the albedo in the SMC. The albedo for the SMC-WG dust was obtained by slightly modifying that of the MW-WG, which was empirically derived from the observations of reflection nebulae. As noted in Draine (2003) and Gordon (2004), the observational estimates of the dust albedo in various regions of the MW appear to be in general agreement with one another at $\lambda^{-1} < 4\ \mu\mathrm{m}^{-1}$. In the wavelength range, the albedo curves of the MW-WD and MW-WG dust are both generally consistent with the observational results within uncertainties. However, at shorter wavelengths, the observational results are sometimes in conflict.

The most important difference between the MW-WD and MW-WG dust models is that the albedo of the MW-WD dust decreases as the wavelength decreases ($\lambda^{-1} > 2\ \ \mu\mathrm{m}^{-1}$), whereas the albedo of the MW-WG dust is more or less constant (Figure 3). As noted in Section 3.1, Seon et al. (2011) found that the scattered FUV continuum background is relatively redder than the direct stellar spectrum. The result was attributed to the increase in scattering albedo with the wavelength, and this supports the wavelength dependence of the albedo of the MW-WD dust type. More detailed radiative transfer modeling of the diffuse FUV background may be required to further understand the albedo curve of the MW dust.

4.2. Correlations with Galaxy Properties

It appears that the UV bump feature is present in typical star-forming galaxies with generally weaker strengths than in the MW extinction curve. The UV strength seems to be associated with galaxy activity. Noll et al. (2009b) found that galaxies with evidence of a UV bump feature host older stellar populations than galaxies lacking an evident bump. It was also shown that more active galaxies with higher specific star formation rates (SFRs) tend to have weaker UV bumps (Wild et al. 2011; Buat et al. 2012; Kriek & Conroy 2013).

This trend can be explained by one of the following scenarios or by combinations of them: (1) variations in the grain size distribution, (2) age-dependent extinction, and (3) radiative transfer effects. First of all, variations in the grain size distribution can cause the trends. The balance between grain formation, growth, and destruction would be altered by star

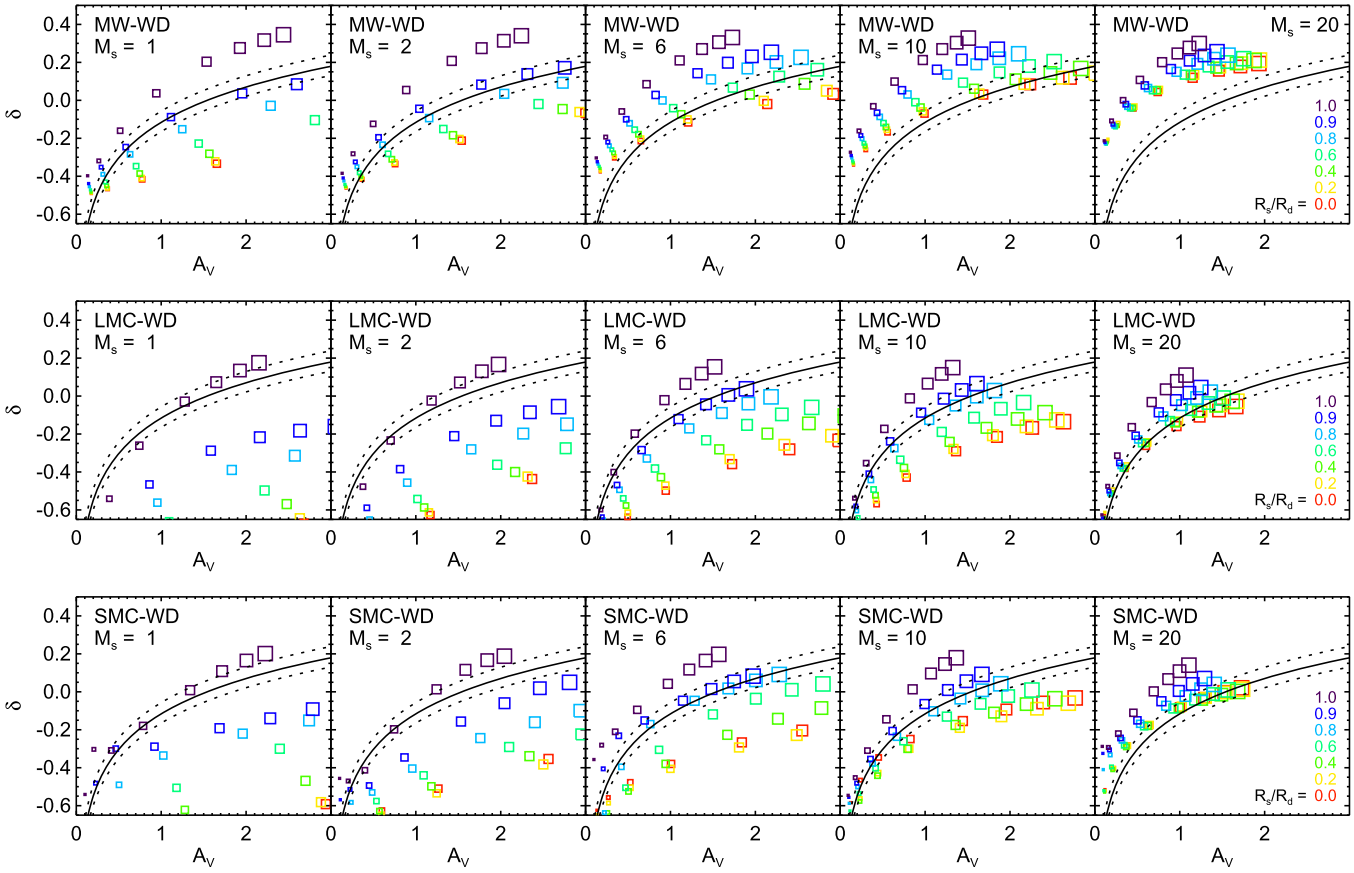

Figure 25. Correlation between the attenuation curve slope δ and A_V for (top) the MW, (middle) LMC, and (right) SMC dust types of Weingartner & Draine (2001). The solid curve shows the δ vs. A_V curve calculated from Equation (10) assuming $A_V = 4.05E(B-V)$ as in the Calzetti curve. The dotted curves are upper and lower bounds defined by $R_V = 4.05 \pm 0.80$. See also the caption of Figure 24 for further explanation.

formation activity; small dust grains can be easily destroyed in active galaxies (e.g., Gordon et al. 2003). Lack of small dust grains or PAHs in active galaxies would yield a weak UV bump as well as a shallower attenuation curve. This is in qualitative agreement with the observational findings. On the other hand, an increased rate of grain shattering in grain-grain collisions could conceivably augment the population of very small grains in active galaxies.

Second, the observed trend might also be ascribed to the age-dependent extinction model, in which old stars are attenuated only by the diffuse ISM, while younger stars experience a higher attenuation that is due to molecular clouds in addition to the diffuse ISM (Granato et al. 2000; Panuzzo et al. 2007). In the models of Granato et al. (2000) and Panuzzo et al. (2007), the attenuation curves for young stars in dense molecular clouds showed very weak UV bumps. However, we found no significant change in attenuation curves when stars are located only within high-density regions, as described in Section 3.5. In the age-dependent extinction model (set B) of Panuzzo et al. (2007), the optical depth of molecular clouds was assumed to be $\tau_{\rm MC} = 20$ at 1 μm, corresponding to $\tau_{\rm MC} \approx 50$ at V band (for the MW dust). As noted in Section 3.5 and by Witt & Gordon (2000), radiative transfer models with such high optical depths can produce attenuation curves with virtually no UV bump. However, the attenuation curves will be much shallower than the Calzetti curve. It is not clear that the slope of the attenuation curves derived in Granato et al. (2000) and Panuzzo et al. (2007) are consistent with the slope of the Calzetti curve. Moreover, as noted in Chevallard et al. (2013), Granato et al. (2000) and Panuzzo et al. (2007) assumed isotropic scattering in solving the radiative equation for a spherically symmetric molecular cloud of uniform density (see Granato & Danese 1994). The approximation of isotropic scattering produces even shallower attenuation curves with a much weaker UV bump at high optical depths as considered in their models.

Finally, we note that radiative transfer effects can also explain the trend. The ISM in more active star-forming galaxies would likely be more clumped, leading to shallower attenuation curves with weaker UV bumps. The observational data in Figure 2 of Kriek & Conroy (2013) show evidence of a correlation between the slope (δ) and A_V. This is also an understandable consequence of radiative transfer effects, as shown in Figure 22. In this interpretation, weaker UV bump strengths and shallower attenuation curves in more active galaxies do not necessarily indicate more effective destruction of the UV bump carriers, but could instead be explained by having a more clumpy ISM and larger dust optical depths in these systems. However, the abundance of the UV bump carriers in the galaxy samples of Kriek & Conroy (2013) should be ~30% or 40% of that of the MW-WD dust. The reduced strength of the UV bump should be useful in constraining the size distribution of dust grains and the dust chemical composition.

A dependence of the attenuation curves on galaxy inclination angle has been observed. Highly inclined galaxies or edge-on

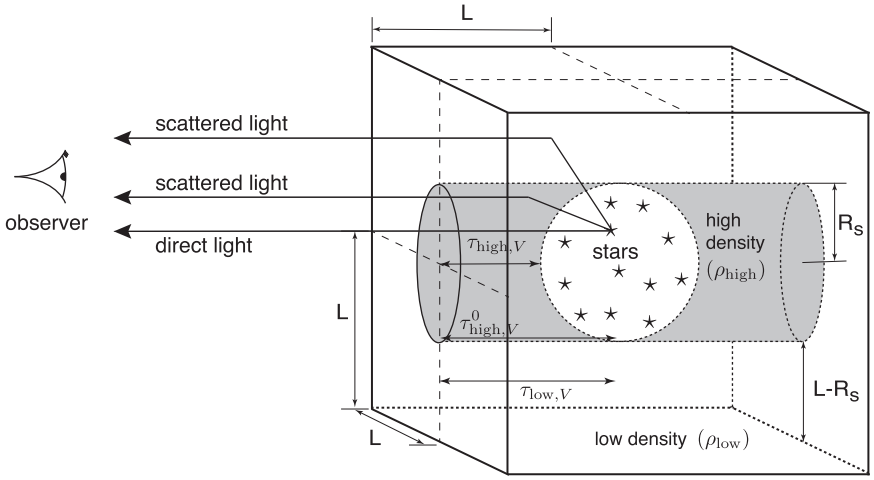

Figure 26. Scattering-dominant geometry. Direct starlight from a spherical region with a radius of R_s is attenuated by a dense cylinder with the same radius R_s. Starlight is scattered not only by the high-density cylindrical region, but also by a low-density region outside of the high-density region and measured by an observer. The optical depths of the low- and high-density media are defined by $\tau_{{\rm low},V} = \kappa_V \rho_{\rm low} L$ and $\tau_{{\rm high},V} = \kappa_V \rho_{\rm high}(L - R_s)$, respectively, where $\rho_{\rm low}$ and $\rho_{\rm high}$ are densities of the media and κ_V is the extinction coefficient at V band. An additional variable $\tau^0_{{\rm high},V}$ is also defined by $\kappa_V \rho_{\rm low} L$ to represent the optical depth in the high-density medium at the limit of $R_s = 0$. There is no dust in the source region.

galaxies tend to have stronger UV bumps (Wild et al. 2011; Kriek & Conroy 2013). However, there seem to be conflicting results with regard to the shape of attenuation curves. Wild et al. (2011) found grayer or shallower attenuation curves for highly inclined galaxies. In radiative transfer calculations for a model late-type galaxy, Pierini et al. (2004) found shallower curves with weaker UV bumps for highly inclined galaxies. In contrast, Kriek & Conroy (2013) observed a weak tendency of steeper attenuation curves for edge-on galaxies. Salmon et al. (2016) found no correlation between the attenuation curve shape and the axis ratios (inclinations) of galaxies.

We can expect a dependence of attenuation curves on inclination angle from our results, even though the present study did not consider detailed geometries of disk galaxies. The vertical scaleheight of dust in disk galaxies is comparable to that of young stars and smaller than that of old stars, but the dust radial scalelength parallel to the major axis is larger than those of stars (e.g., Xilouris et al. 1997; Bianchi 2007; Seon et al. 2014). Therefore, in edge-on galaxies, stars, especially young stars responsible for UV light, will be hidden behind the radially extended dust layer. This configuration is similar to a geometry with $R_s/R_d < 1$ in our model. On the other hand, the star/dust geometry for face-on galaxies will be close to the case with $R_s/R_d \geqslant 1$. The geometry with $R_s/R_d = 1$ for face-on galaxies would give rise to slightly shallower attenuation curves with weaker UV bumps than that with $R_s/R_d < 1$ for edge-on galaxies if the optical depths viewed face-on and edge-on were the same. However, the increase in the optical depth at high inclination angles would yield much stronger (opposite) effects on the attenuation curves than are due to the difference in the star/dust geometry, as shown, for instance, in Figure 22. In the right panels of Figure 22, the variation in E_b and δ that is due to change in R_s/R_d (represented by symbol size) is relatively small compared to the variation due to the τ_V change (represented by color). The same trend was also noted in Section 3.2. Consequently, edge-on galaxies would have shallower attenuation curves with weaker UV bumps. This expectation is consistent with the conclusion obtained with radiative transfer calculations for a disk galaxy in Pierini et al. (2004), but seems not to agree with the observational results of Wild et al. (2011) and Kriek & Conroy (2013). Note that our models and those of Pierini et al. (2004) are complementary in the sense that we assumed a spherical, clumpy ISM, but Pierini et al. (2004) assumed a smooth disk + bulge geometry. For the same reason, both models have limitations in explaining the inclination angle dependence of the attenuation curve. We therefore need to investigate more realistic models incorporating both the clumpiness of ISM and the disk + bulge geometry of galaxies to better understand the observed dependence of the attenuation curve on inclination angle. More systematic observational studies on the inclination angle dependence of the attenuation curve are also required.

4.3. Scattering-dominant Geometry

A geometrical configuration in which single-scattered light dominates direct starlight or scattered light is selectively observed could produce a UV bump-less attenuation curve. One example of the scattering-dominant geometry can be found in halos of edge-on galaxies (e.g., Seon et al. 2014; Shinn & Seon 2015). Figure 26 illustrates a simplified geometry to represent a scattering-dominant configuration, in which the direct starlight from a sphere with a radius R_s is attenuated by a cylindrical dense medium with the same radius and the scattered light from a low-density medium outside the cylinder is substantial. The spherical volume containing stars is carved out to contain no dust, and starlight is not absorbed within the source region. The height of the cylindrical medium is defined by $2L$, as shown in Figure 26. The optical depths of the low- and high-density medium at V band are defined by $\tau_{{\rm high},V} \equiv \kappa_V \rho_{\rm high}(L - R_s)$ and $\tau_{{\rm low},V} \equiv \kappa_V \rho_{\rm low} L$, respectively. We also define an additional variable $\tau^0_{{\rm high},V} \equiv \kappa_V \rho_{\rm high} L = \tau_{{\rm high},V}(R_s = 0)$, which is more appropriate to represent the dust density of the high-density medium. Here, $\rho_{\rm high}$ and $\rho_{\rm low}$ are the densities of high- and low-density medium, respectively, and κ_V is the extinction opacity at V band. Monte Carlo radiative transfer modeling has been perfomred for this geometry by assuming the MW-WD dust model. Figure 27 shows the resulting attenuation curves obtained by fixing $\tau_{{\rm low},V}$ to be

0.05 and varying $\tau^0_{\mathrm{high},V}$ from 1 to 9 in steps of 1. The top and bottom panels show the results for $R_s/L = 0.2$ and 0.5, respectively. The best-fit modified Calzetti curves for the attenuation curves are also shown in the right panels.

In Figure 27 the $E(\lambda - V)/E(B - V)$ and A_λ/A_V curves are both close to the overall shape of the Calzetti curve or the modified Calzetti curve. Note that these attenuation curves for the scattering-dominant geometry were calculated by measuring the flux at a single (edge-on) direction along the cylinder axis, while all the other attenuation curves presented in this paper were obtained by averaging over all directions. Therefore, the attenuation optical depths in Figures 27 and 28 were calculated as $\tau_\lambda^{\mathrm{att}} = -\ln(4\pi\tilde{f}_\lambda^{\mathrm{esc}})$, where $\tilde{f}_\lambda^{\mathrm{esc}}$ is the output SED per unit solid angle divided by the source SED. As $\tau_{\mathrm{high},V}$ increases, starlight from the high-density region is more effectively blocked and the contribution of singly scattered light from the low-density region increases. Because there is no bump feature in the scattering cross section and the optical depth of the low-density scattering medium is very low, the scattering-dominant SEDs lack a UV bump feature at highest $\tau_{\mathrm{high},V}$. However, the UV absorption bump feature appears unless $\tau_{\mathrm{low},V} \ll 1$. As the size of source distribution (R_s) decreases, starlight is more attenuated and shallower attenuation curves with weaker UV bump strengths are obtained. Therefore, the scattering-dominant geometry would at least partly reduce the UV bump strength.

Figure 28 shows the relations between E_b and δ obtained by fitting the attenuation curves for $R_s/L = 0.1$, 0.2, 0.3, and 0.5 to the modified Calzetti curves, together with the empirical relationship found by Kriek & Conroy (2013) and the best-fit linear function for the MW-WD dust models found in Figure 21. The same densities as in Figure 27 were adopted. As optical depth $\tau_{\mathrm{high},V}$ increases, E_b and δ start to deviate from the relation derived from the MW-WD dust models and become closer to the empirical equation found by Kriek & Conroy (2013). It might be possible to further decrease the UV bump strength by adopting the turbulent ISM density distribution for the high-density cylindrical medium.

Seon et al. (2014) and Shinn & Seon (2015) modeled the scattered FUV light observed above the galactic disk of edge-on galaxies by assuming the dust properties of the MW-WD dust. On the other hand, Hodges-Kluck & Bregman (2014) claimed that the the UV colors measured in halos of edge-on galaxies are consistent with the SMC-type dust, lacking a UV bump. However, the SED shape of the scattered flux is mainly determined by the wavelength dependence of the scattering cross section, which has no UV bump feature (Calzetti et al. 1995; Andriesse et al. 1977). The geometry in Figure 26 is not for edge-on galaxies, but appropriate to demonstrate a case in which substantial scattered starlight is observed. Therefore, the results obtained from the geometry illustrate that edge-on galaxies with only the scattered UV SED data may not be useful for determination of the dust type in the halos without a detailed radiative transfer model.

4.4. UV Bumps in Local Starbursts

It is generally believed that the UV bump feature is very weak or absent in local starburst galaxies because the feature is lacking in the Calzetti curve. The presence of a UV bump in typical star-forming galaxies has been regarded as a significant difference from the starburst galaxies. However, we now argue

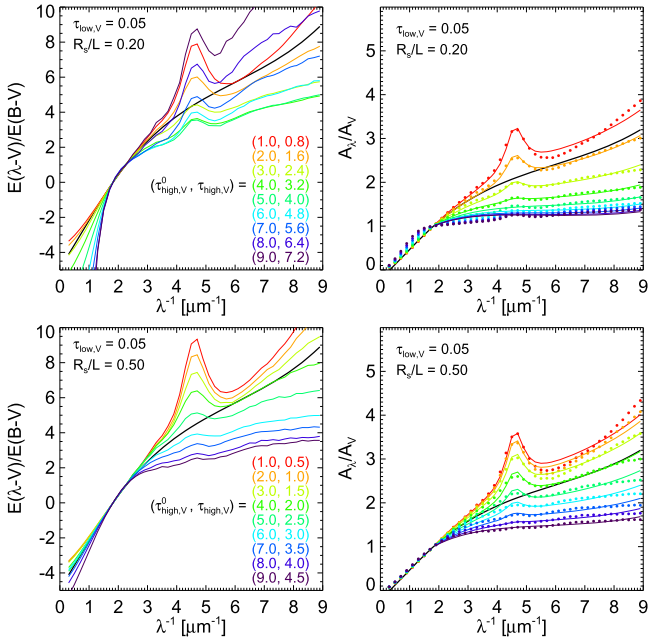

Figure 27. Attenuation curves calculated for the scattering-dominant geometry shown in Figure 26. The optical depth of the high-density region ($\tau_{\mathrm{high},V}$) was varied such that $\tau^0_{\mathrm{high},V}(=\kappa_V \rho_{\mathrm{high}} L) = 1, 2, \cdots, 9$, while the optical depth of the low-density region ($\tau_{\mathrm{low},V}$) was fixed to 0.05. Both $\tau^0_{\mathrm{high},V}$ and $\tau_{\mathrm{high,V}}$ are shown in parentheses for convenience. The top and bottom panels show the attenuation curves for $R_s/L = 0.2$ and 0.5, respectively. The left and right panels show the results in two forms, e.g., $E(\lambda - V)/E(B - V)$ and A_λ/A_V, respectively. In the right panels, the attenuation curves are shown as filled circles and the best-fit modified Calzetti curves are overplotted as lines with the same colors as the circles. The MW-WD dust is assumed for the model calculations. The black curves are the Calzetti curves.

that the local starburst galaxies may not be so different from more normal star-forming galaxies.

Scoville et al. (2015) carefully selected high-redshift galaxies, which are assumed to resemble local starburst galaxies. The authors presented average attenuation curves in two redshift bins ($z = 2$–4 and 4–6.5) normalized to attenuation at $\lambda = 0.13\,\mu$m. The attenuation curves for the two redshift bins are reproduced in the first panel of Figure 29. In order to compare their results with the Calzetti curve and our results, we renormalized the attenuation curves to the values at V band. The renormalized A_λ/A_V curves are shown in the second panel of Figure 29. From the figure, it is now clear that the curve resembles the attenuation curves shown in Figures 8 and 17. The red ($z = 4$–6.5) and green ($z = 2$–4) curves are quite similar to the attenuation curves calculated for low and high optical depths, respectively, in the figures. To derive the UV bump strength, the modified Calzetti curve (Equation (6)) was applied to the data. The lower redshift data were well fit by the parameters of $(\delta, E_b) = (0.13, 0.73)$, which is consistent with the relation between (δ, E_b) given by Kriek & Conroy (2013). The higher redshift data were also found to be comparable with a modified Calzetti curve with $(\delta, E_b) \sim (-0.06, 1.4)$. This implies that the Scoville et al. attenuation curves are consistent with those of Kriek & Conroy (2013). The two modified Calzetti curves that represent the Scoville et al. attenuation curves are shown as dotted lines in the second panel. The Scoville et al. curves are plotted in the $A_\lambda/E(B - V)$ form in the third panel. The lower-redshift curve has a lower $E(B - V)$ color excess than the higher-redshift curve, which led to higher $A_\lambda/E(B - V)$ in the

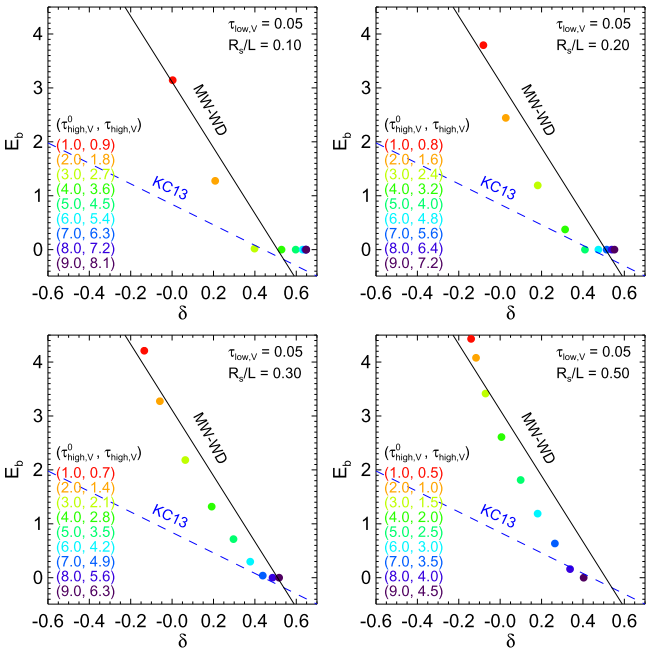

Figure 28. Best-fit results to the modified Calzetti curves for the attenuation curves calculated in the scattering-dominant geometry (Figures 26 and 27). The best-fit bump strength (E_b) and slope (δ) for the models with four radii of the blocking cylinder ($R_s/L = 0.1$, 0.2, 0.3, and 0.5) are compared. As in Figure 27, $\tau^0_{\rm high,V}$ was varied from 1 to 9 in steps of 1 and $\tau_{\rm low,V}$ was fixed to 0.05. The blue dashed line labeled KC13 is the empirical linear relationship found by Kriek & Conroy (2013). The black line labeled MW-WD is the best-fit linear function for the MW-WD dust found in Figure 21.

lower-redshift curve. The property that the order of A_λ/A_V curves is reversed in the $A_\lambda/E(B-V)$ curve was found in Section 3.2.

To derive an average attenuation curve for the *IUE* sample of local starburst galaxies, Calzetti et al. (1994) sorted the sample galaxies according to Balmer decrement bins, averaged the galactic spectra F_ν in each bin, and then divided the spectra by the spectrum showing the lowest extinction. Then, the log ratios were divided by the color excess estimated from the Balmer decrement. The resulting reddening curves were used to derive a final attenuation curve. The template spectra for each Balmer decrement bin[5] were downloaded to compare with the present results. The four template spectra were smoothed with a Gaussian function and are shown in the fourth panel of Figure 29, in which spiky and/or broad features except for the feature at $\lambda^{-1} \sim 4.6\ \mu{\rm m}^{-1}$ are strong atomic absorption lines, such as Hα 6564 Å and C IV $\lambda\lambda$ 1551 Å. We note that the two curves denoted by red and green colors are fairly similar to the Scoville et al. curves with the same colors in the second panel, suggesting that the two template curves have a UV bump strength similar to that of the Scoville et al. curves, although the other template curves show no evidence of a UV absorption bump. Thereby, we can conclude that at least two of the four template spectra of the local starburst galaxies have (weak) UV bumps comparable to other star-forming galaxies, even though there is no UV bump in the Calzetti et al. (1994) overall curve.

UV continuum slopes are also useful in testing for the presence of UV bumps in spectra of local starburst galaxies. Noll & Pierini (2005) divided the UV wavelength range 1200–2500 Å into several subranges and parameterized the UV SEDs of their own sample galaxies observed at $z \sim 2$ and the *IUE* spectra of the local starburst galaxies analyzed in Calzetti et al. (1994) with a power law ($F_\nu \propto \lambda^\beta$) in each subrange. They compared the observational data with the radiative transfer models of Witt & Gordon (2000). In particular, the slopes β, γ_3, and γ_4 defined in wavelength ranges of 1268–1740, 1920–2175, 2175–2480 Å, respectively (see their Table 4 for the precise definitions of the wavelength windows), were used to identify the presence of the UV bump feature. A derived parameter $\gamma_{34} \equiv \gamma_3 - \gamma_4$ measures the curvature of the UV continuum across the UV bump and is very sensitive to the presence of the UV bump feature.

Figure 30 shows the plot of γ_{34} versus β estimated from our radiative transfer calculations for the MW-WD dust with varying strength of the UV bump (f_b, defined relative to the MW extinction curve). In the figure, a change in the UV bump strength is denoted by different colors. The models with varying strength of the whole PAH feature (including both the UV bump and FUV extinction rise) showed no significant difference from those with varying only the UV bump strength and thus are not displayed in this paper. This is because the slope parameters are less sensitive to variation in the FUV extinction rise component. The results for the LMC-WD and SMC-WD dust types are also overplotted with plus (+) and cross (×) symbols, respectively. The loci of the Calzetti curve with a varying UV bump strength are denoted by the near-vertical blue line. The result for the modified Calzetti curve is also shown by the black line adopting the relation between the bump strength and the attenuation curve slope of Kriek & Conroy (2013). Both lines show variation as the bump strength (E_b) increases from 0 (high γ_{34}) to 2 (low γ_{34}). Note that the result obtained for the modified Calzetti curve is consistent with that for MW-WD dust with bump strength suppressed by $f_b \approx 0.2$–0.3, consistent with the results in Figure 22. In calculating γ_{34} and β values for the models, we assumed the stellar continuum slope parameters to be $\gamma_{34} = 1.29$ and $\beta = -2.44$ estimated from the stellar population synthesis model of Maraston (2005) with solar metallicity, standard Salpeter initial mass function, and continuous star formation during an age of 500 Myr. The *IUE* sample of local starburst galaxies and the samples of $z \sim 2$ galaxies are denoted by stars and circles, respectively. The loci occupied by the MW-WD dust type ($f_b = 1$) are slightly shifted to higher β values than those calculated with the MW-WG dust in Noll & Pierini (2005). For the SMC-WD dust type, γ_{34} increases with β. However, for the SMC-WG dust, γ_{34} remains somewhat constant ($\sim$1) as β increases. It is clear that about half of the *IUE* sample galaxies can be described by the MW-WD dust models with weak UV bumps, rather than by the SMC-WD dust. This strengthens the previous conclusion that at least some of the *IUE* starburst galaxies have a UV bump, although it is weaker than that of the MW-WD dust. The mean slopes of $\langle\beta\rangle = -1.05$ and $\langle\gamma_{34}\rangle = 0.27$ are closer to the values obtained from a UV bump-less model of the MW-WD dust than with the SMC-WD dust model. However, the slope parameter γ_{34} ($\sim$1) for the Calzetti curve with no UV bump is more consistent with those of the models obtained from the SMC-WD dust. Note also that no significant difference is found between the distributions of the slopes for the local starburst galaxies and the galaxies at $z \sim 2$, implying the similarity between the local starburst galaxies and the high-redshift galaxies at $z \sim 2$. There are minor changes in β among the various synthesis models

[5] http://www.stsci.edu/hst/observatory/crds/cdbs_kc96.html

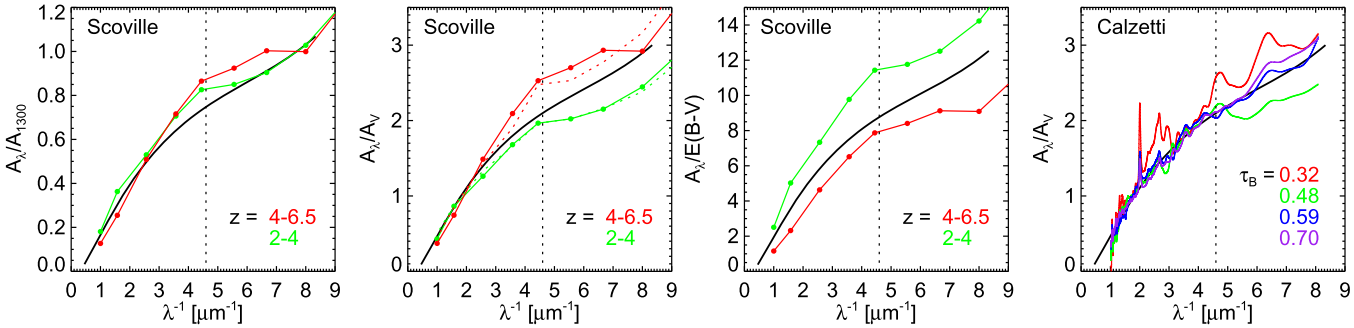

Figure 29. Comparison of the two attenuation curves of high-redshift galaxies in Scoville et al. (2015) and those derived from the four template spectra of local starburst galaxies in Calzetti et al. (1994). The first to third panels show the Scoville et al. attenuation curves normalized to A_{1300}, A_V, and $E(B-V)$, respectively. The last panel shows the attenuation curves derived from the template spectra of local starburst galaxies, after being smoothed with a Gaussian function. The features in the last panel, except for the 2175 Å bump, are atomic lines. The dashed lines in the second panel are for the modified Calzetti law (Equation (6)). In each panel, the black line is the Calzetti curve.

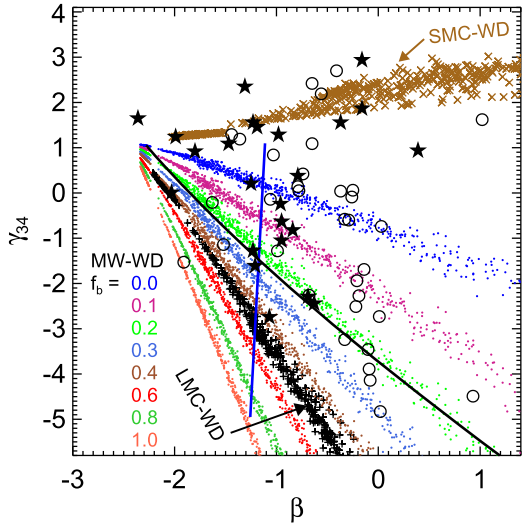

Figure 30. Relation between the slope parameters γ_{34} and β. The UV bump strength (f_b) for the MW-WD dust type was varied from 0 to 1.0. The results for the SMC-WD and LMC-WD dust types are also shown as brown cross ($\times$) and black plus ($+$) symbols, respectively. The blue vertical line denotes the result calculated for the Calzetti curve + UV bump with a varying strength. The black line shows the result for the modified Calzetti curve, adopting the $E_b - \delta$ relation of Kriek & Conroy (2013). In both cases, the bump strength E_b increases from 0 ($\gamma_{34} \approx 1$) to 2 ($\gamma_{34} \approx -5$). The *IUE* data for 24 local starburst galaxies and the Focal Reducer and Spectrograph Deep Field (FDF) data for the galaxies at $z \sim 2$ were taken from Noll & Pierini (2005) and are shown as stars and circles, respectively.

considered in Noll & Pierini (2005), but this does not alter our conclusion.

In Figure 30 the slope parameters for the LMC-WD dust are similar to those of the MW-WD dust models with a bump strength of ∼0.5. This suggests that the overall distribution of the slope parameters for the galaxies in the figure may be equivalently reproduced by the LMC-WD dust if its UV bump strength were varied. However, the overall shape of the A_λ/A_V attenuation curves derived from the LMC-WD dust are in general steeper than the Calzetti curve, as shown in Figure 9. As noted in Section 3.2, the shape of the Calzetti curve was better consistent with those of the MW-WD attenuation curves over a wider range of model parameters than those of the LMC-WD dust. Therefore, most of the calculations in the present study were based on the MW-WD dust extinction curve.

Using the *IUE* and *IRAS* data for local starburst galaxies, Meurer et al. (1999) proposed a formula to estimate dust attenuation from a UV spectral slope β (this is different from β in Noll & Pierini 2005), based on the tight relation between the IR to UV flux ratio (referred to as the infrared excess, IRX) and β. However, it has been observed that star-forming galaxy samples selected at optical and UV wavelengths are located significantly below the IRX-β relation of Meurer et al. (1999) (e.g., Buat et al. 2005; Boissier et al. 2007). Takeuchi et al. (2012) found that the UV fluxes in Meurer et al. (1999) were significantly underestimated because of the small aperture of the *IUE* ($10'' \times 20''$), and that consequently, their IRX values were overestimated. The aperture size effect led to the IRX-β relation being shifted upward on the plot. Takeuchi et al. (2012) calibrated the UV fluxes for the local starburst galaxies with the *GALEX* data and derived a revised IRX-β relation, which is shifted downward compared to that of Meurer et al. (1999). The new relation was then found to be consistent with the star-forming galaxy samples. This seems to suggest that the attenuation properties of local starburst galaxies are in fact similar to those of other star-forming galaxies. However, this does not directly indicate the existence of a UV bump in local starburst galaxies. In a future study, it may be worthwhile to apply the modified Calzetti curve to the *IUE* spectral data of local starburst galaxies together with the recent photometric data of *GALEX* and the *Swift* UVOT to better understand the attenuation curves in local starburst galaxies.

5. SUMMARY

The dust attenuation curves of starlight in galactic environments were investigated through Monte Carlo radiative transfer models, which employ dust density distributions appropriate for a clumpy ISM. The full numerical results of the models are made available to the community via the authors' WWW site.[6]

The principal conclusions of this paper that confirm previous works (e.g., Witt & Gordon 2000; Pierini et al. 2004, etc) are as follows:

1. It is confirmed that the absolute amount of dust is not well determined by the color excess $E(B-V)$ that is due to the saturation of $E(B-V)$.
2. Theoretically derived attenuation curves show large variations in both the curve slope and the UV bump strength, depending on the star/dust geometry, clumping, and total amount of dust.

[6] http://seoncafe.github.io/MoCafe.html

3. The correlation between the slope and the $E(B-V)$ color as found in Salmon et al. (2016) can be explained by radiative transfer effects; as optical depth increases, attenuation curves become shallower and redder.
4. The attenuation curves become grayer (or shallower) and the strength of the 2175 Å absorption bump becomes weaker as the optical depth, the clumping, and the size of source distribution increase.

The principal conclusions that are newly found in this paper are as follows:

1. Scattering at $\lambda^{-1} \gtrsim 2\ \mu\mathrm{m}^{-1}$ can lead to either reddening or blueing, depending on the wavelength dependence of the albedo. We note that the blueing of the scattered light at optical wavelengths was shown in Witt & Gordon (2000). However, the fact that the reddening or blueing is determined by the albedo curve has not previously been investigated.
2. The shape of the attenuation curves is primarily determined by the wavelength dependence of absorption rather than by the extinction (absorption + scattering) curve.
3. Attenuation curves consistent with the original Calzetti curve (Calzetti et al. 1994, 2000) are obtained using the MW dust model of Weingartner & Draine (2001), provided the 2175 Å absorption bump is partially or totally suppressed.
4. The discrepancy between our results and previous studies that claimed SMC-type dust to be the most likely origin of the Calzetti curve is mainly attributed to the differences in the adopted dust albedo and the strength of the 2175 Å bump; this study uses the theoretically calculated albedos and suppresses the bump strength, whereas previous studies used empirically estimated albedos and the bump strength fixed to that of the MW extinction curve.
5. The model attenuation curves are generally well represented by the modified Calzetti curve (Equation (6)) proposed by Noll et al. (2009a) to allow variation in the attenuation curve slope and UV bump strength. Note that Noll et al. (2009a), Buat et al. (2011, 2012), and Kriek & Conroy (2013) found that the observational data are better described by the modified Calzetti curve than by the original Calzetti curve.
6. The correlation between the slope and UV bump strength (Equation (9)), with steeper curves having stronger bumps, as found in a large sample of star-forming galaxies (Kriek & Conroy 2013), is well reproduced when the abundance of the UV bump carriers or PAHs is assumed to be 30% or 40% of that of the MW dust.
7. The correlation between the slope and UV bump strength found by Kriek & Conroy (2013) is explained by radiative transfer effects, which lead to shallower attenuation curves with weaker UV bumps as the ISM is more clumpy and has a higher dust mass.
8. It is demonstrated that a scattering-dominant geometry in which direct starlight is mostly absorbed and single-scattered light dominates the direct starlight can produce attenuation curves with a very weak UV bump and with a shallow slope.
9. It is also shown that at least some of the local starburst galaxies appear to have a UV bump feature in their attenuation curves, although it is much weaker than the bump of the MW dust.

Numerical simulations were partially performed by using a high-performance computing cluster at the Korea Astronomy and Space Science Institute. B.T.D. was supported in part by NSF grant AST-1408723.

REFERENCES

Allain, T., Leach, S., & Sedlmayr, E. 1996, A&A, 305, 602
Amanatides, J., & Woo, A. 1987, in Proc. Eurographics '87, ed. G. Marechal (New York: Elsevier), 3
Andriesse, C. D., Piersma, T. R., & Witt, A. N. 1977, A&A, 54, 841
Baes, M., Gordon, K. D., Lunttila, T., et al. 2016, A&A, 590, A55
Baes, M., Verstappen, J., De Looze, I., et al. 2011, ApJS, 196, 22
Barnes, J. E., Wood, K., Hill, A. S., & Haffner, L. M. 2015, MNRAS, 447, 559
Battisti, A. J., Calzetti, D., & Chary, R. R. 2016, ApJ, 818, 13
Berkhuijsen, E. M., Berkhuijsen, E. M., Fletcher, A., & Fletcher, A. 2015, MNRAS, 448, 2469
Berkhuijsen, E. M., & Fletcher, A. 2008, MNRAS, 390, L19
Bianchi, L., Clayton, G. C., Bohlin, R. C., Hutchings, J. B., & Massey, P. 1996, ApJ, 471, 203
Bianchi, S. 2007, A&A, 471, 765
Bianchi, S., Ferrara, A., Davies, J. I., & Alton, P. B. 2000, MNRAS, 311, 601
Boissier, S., Gil de Paz, A., Boselli, A., et al. 2007, ApJS, 173, 524
Buat, V., Giovannoli, E., Heinis, S., et al. 2011, A&A, 533, A93
Buat, V., Iglesias-Páramo, J., Seibert, M., et al. 2005, ApJL, 619, L51
Buat, V., Noll, S., Burgarella, D., et al. 2012, A&A, 545, A141
Burgarella, D., Buat, V., & Iglesias-Páramo, J. 2005, MNRAS, 360, 1413
Burkhart, B., & Lazarian, A. 2012, ApJL, 755, L19
Calzetti, D. 1997, AJ, 113, 162
Calzetti, D., Armus, L., Bohlin, R. C., et al. 2000, ApJ, 533, 682
Calzetti, D., Bohlin, R. C., Gordon, K. D., Witt, A. N., & Bianchi, L. 1995, ApJL, 446, L97
Calzetti, D., Kinney, A. L., & Storchi Bergmann, T. 1994, ApJ, 429, 582
Cashwell, E., & Everett, C. 1959, A Practical Manual on the Monte Carlo Method for Random Walk Problems (New York: Pergamon)
Charlot, S., & Fall, S. M. 2000, ApJ, 539, 718
Chevallard, J., Charlot, S., Wandelt, B., & Wild, V. 2013, MNRAS, 432, 2061
Clayton, G. C., Gordon, K. D., Bianchi, L. C., et al. 2015, ApJ, 815, 14
Conroy, C. 2010, MNRAS, 404, 247
Conroy, C. 2013, ARA&A, 51, 393
Conroy, C., Schiminovich, D., & Blanton, M. R. 2010, ApJ, 718, 184
Draine, B. T. 2003, ApJ, 598, 1017
Elíasdóttir, Á., Fynbo, J. P. U., Hjorth, J., et al. 2009, ApJ, 697, 1725
Elíasdóttir, Á., Hjorth, J., Toft, S., Burud, I., & Paraficz, D. 2006, ApJS, 166, 443
Elmegreen, B. G. 1997, ApJ, 477, 196
Elmegreen, B. G. 2002, ApJ, 564, 773
Elmegreen, B. G., & Scalo, J. 2004, ARA&A, 42, 211
Federrath, C., Klessen, R. S., & Schmidt, W. 2008, ApJL, 688, L79
Federrath, C., Roman-Duval, J., Klessen, R. S., Schmidt, W., & Mac Low, M. M. 2010, A&A, 512, 81
Fischera, J., & Dopita, M. 2005, ApJ, 619, 340
Fischera, J., & Dopita, M. 2011, A&A, 533, 117
Fischera, J., Dopita, M. A., & Sutherland, R. S. 2003, ApJL, 599, L21
Fitzpatrick, E. L. 1999, PASP, 111, 63
Fitzpatrick, E. L., & Massa, D. 1986, ApJ, 307, 286
Fitzpatrick, E. L., & Massa, D. 2007, ApJ, 663, 320
Frigo, M., & Johnson, S. G. 2005, in Proc.of the IEEE Vol. 93, Program Generation, Optimization, and Platform Adaptation, ed. J. Moura, M. Puschel, J. Dongarra, & D. Padua (Piscataway, NJ: IEEE), 216
Froebrich, D., & Rowles, J. 2010, MNRAS, 406, 1350
Gordon, K. D. 2004, in ASP Conf. Ser. 309, Astrophysics of Dust, ed. A. N. Witt, G. C. Clayton, & B. T. Draine (San Francisco, CA: ASP), 77
Gordon, K. D., Calzetti, D., & Witt, A. N. 1997, ApJ, 487, 625
Gordon, K. D., & Clayton, G. C. 1998, ApJ, 500, 816
Gordon, K. D., Clayton, G. C., Misselt, K. A., Landolt, A. U., & Wolff, M. J. 2003, ApJ, 594, 279
Gordon, K. D., Gordon, K. D., Hanson, M. M., et al. 1999a, ApJ, 519, 165
Gordon, K. D., Misselt, K. A., Witt, A. N., & Clayton, G. C. 2001, ApJ, 551, 269

Gordon, K. D., Smith, T. L., & Clayton, G. C. 1999b, in ASP Conf. Ser. 193, The Hy-Redshift Universe: Galaxy Formation and Evolution at High Redshift, ed. A. J. Bunker & W. J. M. van Breugel (San Francisco, CA: ASP), 517
Granato, G. L., & Danese, L. 1994, MNRAS, 268, 235
Granato, G. L., Lacey, C. G., Silva, L., et al. 2000, ApJ, 542, 710
Hagen, L. M. Z., Siegel, M. H., Gronwall, C. A., et al. 2015, arXiv:1504.06635
Hodges-Kluck, E., & Bregman, J. N. 2014, ApJ, 789, 131
Holwerda, B. W., Böker, T., Dalcanton, J. J., Keel, W. C., & de Jong, R. S. 2013, MNRAS, 433, 47
Holwerda, B. W., & Keel, W. C. 2013, A&A, 556, 42
Hoversten, E. A., Gronwall, C., Vanden Berk, D. E., et al. 2011, AJ, 141, 205
Ilbert, O., Capak, P., Salvato, M., et al. 2009, ApJ, 690, 1236
Inoue, A. K. 2005, MNRAS, 359, 171
Inoue, A. K., Buat, V., Burgarella, D., et al. 2006, MNRAS, 370, 380
Johnson, B. D., Schiminovich, D., Seibert, M., et al. 2007, ApJS, 173, 392
Jones, A. P., Tielens, A. G. G. M., Hollenbach, D. J., & McKee, C. F. 1994, ApJ, 433, 797
Kauffmann, G., Heckman, T. M., White, S. D. M., et al. 2003, MNRAS, 341, 33
Kennicutt, R. C. J. 1998, ARA&A, 36, 189
Kim, J., & Ryu, D. 2005, ApJL, 630, L45
Kinney, A. L., Calzetti, D., Bica, E., & Storchi Bergmann, T. 1994, ApJ, 429, 172
Klessen, R. S. 2000, ApJ, 535, 869
Kriek, M., & Conroy, C. 2013, ApJL, 775, L16
Kriek, M., van Dokkum, P. G., Whitaker, K. E., et al. 2011, ApJ, 743, 168
Kritsuk, A. G., Norman, M. L., & Padoan, P. 2006, ApJL, 638, L25
Kurosawa, R., & Hillier, D. J. 2001, A&A, 379, 336
Leitherer, C., Li, I.-H., Calzetti, D., & Heckman, T. M. 2002, ApJS, 140, 303
Li, A., & Draine, B. T. 2001, ApJ, 554, 778
Li, A., & Draine, B. T. 2002, ApJ, 572, 232
Lillie, C. F., & Witt, A. N. 1976, ApJ, 208, 64
Lombardi, M., Lada, C. J., & Alves, J. 2008, A&A, 489, 143
Maraston, C. 2005, MNRAS, 362, 799
Marsaglia, G., & Zaman, A. 1993, The KISS generator, Technical report, Department of Statistics (Tallahassee, FL: Univ. Florida)
Massarotti, M., Iovino, A., Buzzoni, A., & Valls-Gabaud, D. 2001, A&A, 380, 425
Mathis, J. S., Whitney, B. A., & Wood, K. 2002, ApJ, 574, 812
Meurer, G. R., Heckman, T. M., & Calzetti, D. 1999, ApJ, 521, 64
Micelotta, E. R., Jones, A. P., & Tielens, A. G. G. M. 2010, A&A, 510, 36
Mishra, A., & Li, A. 2015, ApJ, 809, 120
Misselt, K. A., Clayton, G. C., & Gordon, K. D. 1999, ApJ, 515, 128
Molina, F. Z., Glover, S. C. O., Federrath, C., & Klessen, R. S. 2012, MNRAS, 423, 2680
Morgan, D. H., Nandy, K., & Thompson, G. I. 1976, MNRAS, 177, 531
Nolan, C. A., Federrath, C., & Sutherland, R. S. 2015, MNRAS, 451, 1380
Noll, S., Burgarella, D., Giovannoli, E., et al. 2009a, A&A, 507, 1793
Noll, S., & Pierini, D. 2005, A&A, 444, 137
Noll, S., Pierini, D., Cimatti, A., et al. 2009b, A&A, 499, 69
Noll, S., Pierini, D., Pannella, M., & Savaglio, S. 2007, A&A, 472, 455
Omont, A. 1986, A&A, 164, 159
Ostriker, E. C., Stone, J. M., & Gammie, C. F. 2001, ApJ, 546, 980
Padoan, P., Jimenez, R., Juvela, M., & Nordlund, A. 2004, ApJL, 604, L49
Padoan, P., Jones, B. J. T., & Nordlund, A. P. 1997, ApJ, 474, 730
Panuzzo, P., Granato, G. L., Buat, V., et al. 2007, MNRAS, 375, 640
Pierini, D., Gordon, K. D., Witt, A. N., & Madsen, G. J. 2004, ApJ, 617, 1022
Povich, M. S., Stone, J. M., Churchwell, E., et al. 2007, ApJ, 660, 346
Press, W. H., Teukolsky, S. A., Vetterling, W. T., & Flannery, B. P. 1992, Numerical Recipes in FORTRAN. The Art of Scientific Computing (2ed ed.; New York: Cambridge Univ. Press)
Reddy, N. A., Kriek, M., Shapley, A. E., et al. 2015, ApJ, 806, 259
Reddy, N. A., Steidel, C. C., Pettini, M., et al. 2008, ApJS, 175, 48
Reddy, N. A., Steidel, C. C., Pettini, M., & Bogosavljević, M. 2016, ApJ, 828, 107
Salmon, B., Papovich, C., Long, J., et al. 2016, ApJ, 827, 20
Sawicki, M., & Yee, H. K. C. 1998, AJ, 115, 1329
Scoville, N., Faisst, A., Capak, P., et al. 2015, ApJ, 800, 108
Seon, K.-I. 2009, ApJ, 703, 1159
Seon, K.-I. 2012, ApJL, 761, L17
Seon, K.-I. 2013, ApJ, 772, 57
Seon, K.-I. 2015, JKAS, 48, 57
Seon, K.-I., Edelstein, J., Korpela, E., et al. 2011, ApJS, 196, 15
Seon, K.-I., & Witt, A. N. 2012, ApJ, 758, 109
Seon, K.-I., Witt, A. N., Shinn, J.-H., & Kim, I.-J. 2014, ApJL, 785, L18
Shapley, A. E., Steidel, C. C., Adelberger, K. L., et al. 2001, ApJ, 562, 95
Shinn, J.-H., & Seon, K.-I. 2015, ApJ, 815, 133
Shivaei, I., Reddy, N. A., Steidel, C. C., & Shapley, A. E. 2015, ApJ, 804, 149
Stalevski, M., Fritz, J., Baes, M., Nakos, T., & Popovic, L. C. 2012, MNRAS, 420, 2756
Steidel, C. C., Adelberger, K. L., Giavalisco, M., Dickinson, M., & Pettini, M. 1999, ApJ, 519, 1
Steinacker, J., Baes, M., & Gordon, K. D. 2013, ARA&A, 51, 63
Stutzki, J., Bensch, F., Heithausen, A., Ossenkopf, V., & Zielinsky, M. 1998, A&A, 336, 697
Takeuchi, T. T., Yuan, F.-T., Ikeyama, A., Murata, K. L., & Inoue, A. K. 2012, ApJ, 755, 144
Vazquez-Semadeni, E. 1994, ApJ, 423, 681
Vijh, U. P., Witt, A. N., & Gordon, K. D. 2003, ApJ, 587, 533
Voss, R. F. 1988, in The Science of Fractal Images, ed. H.-O. Peitgen & D. Saupe (New York: Springer)
Weingartner, J. C., & Draine, B. T. 2001, ApJ, 548, 296
Wild, V., Charlot, S., Brinchmann, J., et al. 2011, MNRAS, 417, 1760
Witt, A. N. 1977, ApJS, 35, 1
Witt, A. N., Friedmann, B. C., & Sasseen, T. P. 1997, ApJ, 481, 809
Witt, A. N., & Gordon, K. D. 1996, ApJ, 463, 681
Witt, A. N., & Gordon, K. D. 2000, ApJ, 528, 799
Witt, A. N., & Lillie, C. F. 1973, A&A, 25, 397
Witt, A. N., Petersohn, J. K., Bohlin, R. C., et al. 1992a, ApJL, 395, L5
Witt, A. N., Thronson, H. A. J., & Capuano, J. M. J. 1992b, ApJ, 393, 611
Wolf, S., Henning, T., & Stecklum, B. 1999, A&A, 349, 839
Xilouris, E. M., Kylafis, N. D., Papamastorakis, J., Paleologou, E. V., & Haerendel, G. 1997, A&A, 325, 135
Zeimann, G. R., Ciardullo, R., Gronwall, C., et al. 2015, ApJ, 814, 162